

## Article

# Petrography and Geochemistry of Hydrothermal Alteration in the Low-Sulfidation Epithermal Kestanelik Au Deposit, Biga Peninsula, NW Turkey

Didem Kiray <sup>1,\*</sup>  and Oya Cengiz <sup>2</sup><sup>1</sup> Lider Yonetim OSGB, Çanakkale 17020, Turkey<sup>2</sup> Department of Geological Engineering, Süleyman Demirel University, Isparta 32260, Turkey; oyacengiz@sdu.edu.tr

\* Correspondence: dkiray17@gmail.com; Tel.: +90-286-212-2118

**Abstract:** In this study, the facies and degrees of hydrothermal alteration related to the low-sulfidation epithermal Kestanelik Au deposit in the Biga Peninsula metallogenic province are identified through petrographic studies and analysis of geochemical characteristics, such as mass changes, molar element ratios, and alteration indices. The gold mineralization is located in silicified zones containing veins and stockwork veinlets of silica. In the Kestanelik Au deposit, common hydrothermal alteration is mainly found in the Permian–Upper Cretaceous Çamlıca basement metamorphics and the Eocene granodiorite, and less often in the Eocene Şahinli volcanic rocks of the Karabiga Massif on the Peninsula. Based on mineralogical and geochemical studies conducted on altered samples, four different alteration facies are defined as silicic, sericitic, argillic, and propylitic, which show remarkable differences in the behavior of REEs, Si, K, Al, Na, and Ca elements. The hydrothermal fluids that caused alteration in the Kestanelik Au mineralization and host rocks had low REE contents because of REE mobilization. In addition, the kaolinization of feldspars and micas, and the chloritization of biotite and feldspars, may have caused negative Eu anomalies. The characterization of rocks subjected to hydrothermal alteration that are most influenced by diverse K-metasomatism with the largest K gains and losses in Na–Ca is illustrated by molar element ratio plots. Depending on the intensity of K-metasomatism, gold mineralization increases with increasing K trends toward gold ore veins. In the Kestanelik Au field, the argillic, sericitic, and propylitic alteration types from the zones enclosing the Au ore veins are revealed using the Ishikawa alteration index and chlorite–carbonate–pyrite index. Mass changes in the altered rocks indicate that there are gains in Si, K, and Al, and losses in Na and Ca with the increasing intensity of alteration toward the ore veins. The results confirm the presence of silicic and K–metasomatic (sericite and argillic) and propylitic (Fe-rich chloride) alteration zoning extending from the inner regions to the outer regions, which characterize the epithermal ore systems.



**Citation:** Kiray, D.; Cengiz, O. Petrography and Geochemistry of Hydrothermal Alteration in the Low-Sulfidation Epithermal Kestanelik Au Deposit, Biga Peninsula, NW Turkey. *Minerals* **2024**, *14*, 379. <https://doi.org/10.3390/min14040379>

Academic Editor: Alireza Somarin

Received: 5 March 2024

Revised: 31 March 2024

Accepted: 1 April 2024

Published: 4 April 2024

**Keywords:** Biga Peninsula; low-sulfidation epithermal type; hydrothermal alteration; alteration indices; mass change; molar element ratio; mobility



**Copyright:** © 2024 by the authors. Licensee MDPI, Basel, Switzerland. This article is an open access article distributed under the terms and conditions of the Creative Commons Attribution (CC BY) license (<https://creativecommons.org/licenses/by/4.0/>).

## 1. Introduction

Hydrothermal alteration is common around epithermal mineral deposits, and the alteration types are similar to those found in characteristic epithermal deposits worldwide and in Turkey [1–11]. One of the most crucial features of epithermal gold deposits is that they are always included within the host rock alteration. Alteration occurs in siliceous and clayey zones. Silicification is commonly observed in the upper part of epithermal veins and in their immediate vicinity, while argillization and propylitization are observed in the outer zones [12]. The alteration products are usually quartz, adularia, illite, chlorite, alunite, kaolinite, and/or dickite and sericite [13]. Hydrothermal alteration is one of the most significant features guiding the exploration for epithermal

deposits. Alteration mineralogy can provide valuable information for determining the spatial distribution of hydrothermal regions that can indicate mineralization [14,15]. Therefore, it is important to investigate the mineralogy in alteration zones and specify the relationship between alteration types and mineralization. Hydrothermal alteration styles have been defined using alteration mineral assemblages [16,17]. The alteration types in low-sulfidation epithermal deposits are classified as propylitic, argillic, advanced argillic, silicic, and sericitic types, respectively [13]. For example, the alteration mineral association of quartz  $\pm$  calcite  $\pm$  adularia  $\pm$  illite in low-sulfidation deposits, including Au–Ag, or Ag–Pb–Zn ores [18,19]. Globally, the various alteration types occur at different intensities in the silicified vein [20–23], monzonite [24], diorite porphyry [5,6], granite-granodiorite porphyry [22,25,26], and metamorphic [22,27]–volcanic rocks [8,21,28].

Compared to the wealth published in the literature regarding the research into the origin of epithermal Au–Ag deposits, there are very few detailed clay mineralogy studies on the alteration zones of epithermal deposits [28–34]. In a mineralogical study on the argillic alteration zone in the low-sulfidation epithermal type Ovacık–Bergama Au–Ag deposit, it was noted that telescoping resulted in four episodes of alteration [28]. In nearby areas of the Cerro Rubio kaolin deposit, it was emphasized that identification of the genesis of weathering or hydrothermal alteration is important in gold or kaolin explorations, considering the presence of epithermal deposits showing argillic alteration [30]. The authors of [34] reported that volcanic rocks forming residual kaolin deposits also host significant Au–Ag mineralization and are mainly silicification, argillic, sericitic, and propylitic altered. Phyllosilicate mineralogy is described as a key element in understanding hydrothermal processes within adopted epithermal deposit models. The characteristics of phyllosilicate mineralogy related to hydrothermal alteration assemblages and ore mineralization have also been discussed [29].

Hydrothermal alteration has been investigated in detail concerning major- and minor oxides, trace element and rare earth element contents, mass gain and loss, molar ratio, and alteration indices for some epithermal Au deposits [5,6,8,35–50]. Some researchers [51–54] have suggested that molar ratio plots are effective in the calculation of mass transfer related to hydrothermal alteration systems. Pyrite, sericite, and chlorite–carbonate tend to be associated primarily with argillic and sericite–carbonate–clay minerals in the Siah Jangal–Sar Kahno epithermal Au vein [6]. In the Tarom–Hashtjin precious and base metal epithermal deposit, illite–smectite, illite, K–mica, and K–feldspar–biotite areas indicate argillic, sericitic, and propylitic alteration types, with the presence of K–Al gains [8].

The area of this study encompasses the low-sulfidation epithermal Kestanelik gold deposit and its nearby surroundings within the Karabiga Massif, Biga Peninsula, NW Turkey (Figure 1a,b). Based on the mass changes, molar element ratios, alteration indices, and alteration facies in the silicified vein–veinlet, quartz–feldspar porphyry, and quartz–mica schist host rocks reported in this study, the mineralogy and geochemistry of hydrothermal alteration types related to Kestanelik gold mineralization are characterized in detail for the first time.

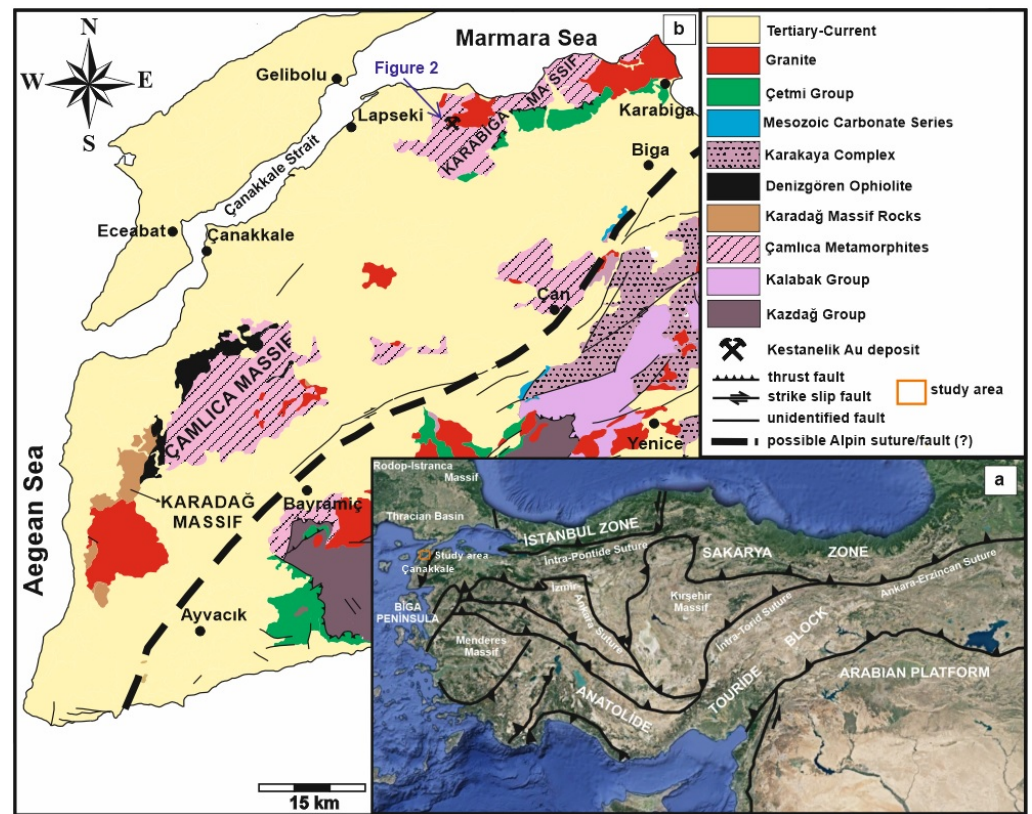


**Figure 1.** (a) Tectonic map of Turkey [55]; (b) geological map showing the generalized geology of the Biga Peninsula [56].

## 2. Regional Geology

With the opening and closing of the Neotethys ocean basin, the Tethyan–Eurasian Metallogenic Belt developed as a result of the occurrence of the Alpine–Himalayan orogeny during the Mesozoic–Cenozoic periods [57]. This belt, extending from Southern Europe in the west to the Western Pacific in the east, is known as one of the richest metal-producing belts in the world [58]. Turkey forms a part of the western region of this large magmatic–metallogenic zone and hosts many precious (Au, Ag) and base-metal (Pb, Zn, Cu) deposits. Western Anatolia, which occupies a significant position in the Alpine–Himalayan orogenic system, is a critical zone where collisional magmatism is abundant, crust–mantle interaction can be observed, and magmatic–tectonic occurrences occur collectively [59,60]. In Turkey, from the east–west trending orogenic belts, there are four primary tectonic blocks, i.e., Pontides, Anatolides, Taurides, and Border folds, from north to south. The northwest of Turkey is bounded by the Intra-Pontide in the north and the Izmir–Ankara–Erzincan Suture Zone in the south (Figure 1a). To the north of this zone is a region known as the Pontides or Sakarya Zone [57,61,62].

Biga Peninsula is one of the areas with the best exposures of the mixed basement rocks of the Alpine tectonic belt, known as the Sakarya Continent [57,63], Sakarya Zone [64], and/or Sakarya Composite Belt [65]. The geology of the Sakarya Zone is generally defined by the Kazdağ, Karadağ, Çamlıca, and Karabiga massifs [64] (Figure 1b). The crystalline basement of the zone is broadly divided into three parts: (i) High-grade Variscan metamorphic succession consisting of gneiss, amphibolite, marble, and rarely metaperidotite—this metamorphism was determined to be Carboniferous (330–310 Ma) with zircon and monazite ages obtained from the Pular, Kazdağ, and Gümüşhane massifs [66,67]; (ii) Paleozoic granitoids of Devonian, Carboniferous, and Permian crystallization age [66–70]; (iii) Permo–Triassic and low-grade Lower Karakaya Complex dominated by metabasite, phyllite, and marble [71]—this complex, which contains Late Triassic blueschist and eclogite,

expresses the Permo–Triassic subduction-accumulation complex [70]. The complex basement is unconformably covered by a sedimentary and volcanic succession of Early Jurassic age, which is represented by shallow marine sandstone, shale, and conglomerate [64]. The Biga Peninsula is the richest Au–Ag and base-metal (Pb, Zn, Cu) mineralization region in Anatolia. The epithermal mineralization is associated with Cenozoic volcanic rocks and Eocene granodiorites belonging to the Sakarya Zone.

### 3. Local Geology

The study area is located within the Karabiga Massif, which is developed in the Sakarya Zone of the Biga Peninsula. In the massif, the Çamlıca metamorphic basement rocks, which are from the Permian to the Upper Cretaceous, and the Çetmi Mélange from the Upper Cretaceous with tectonic contact, are cut by the Kestanelik granodiorite and silicified veins of the Eocene. The Eocene Soğucak Formation, Şahinli Formation, and Quaternary alluviums unconformably overlie these units (Figure 2).

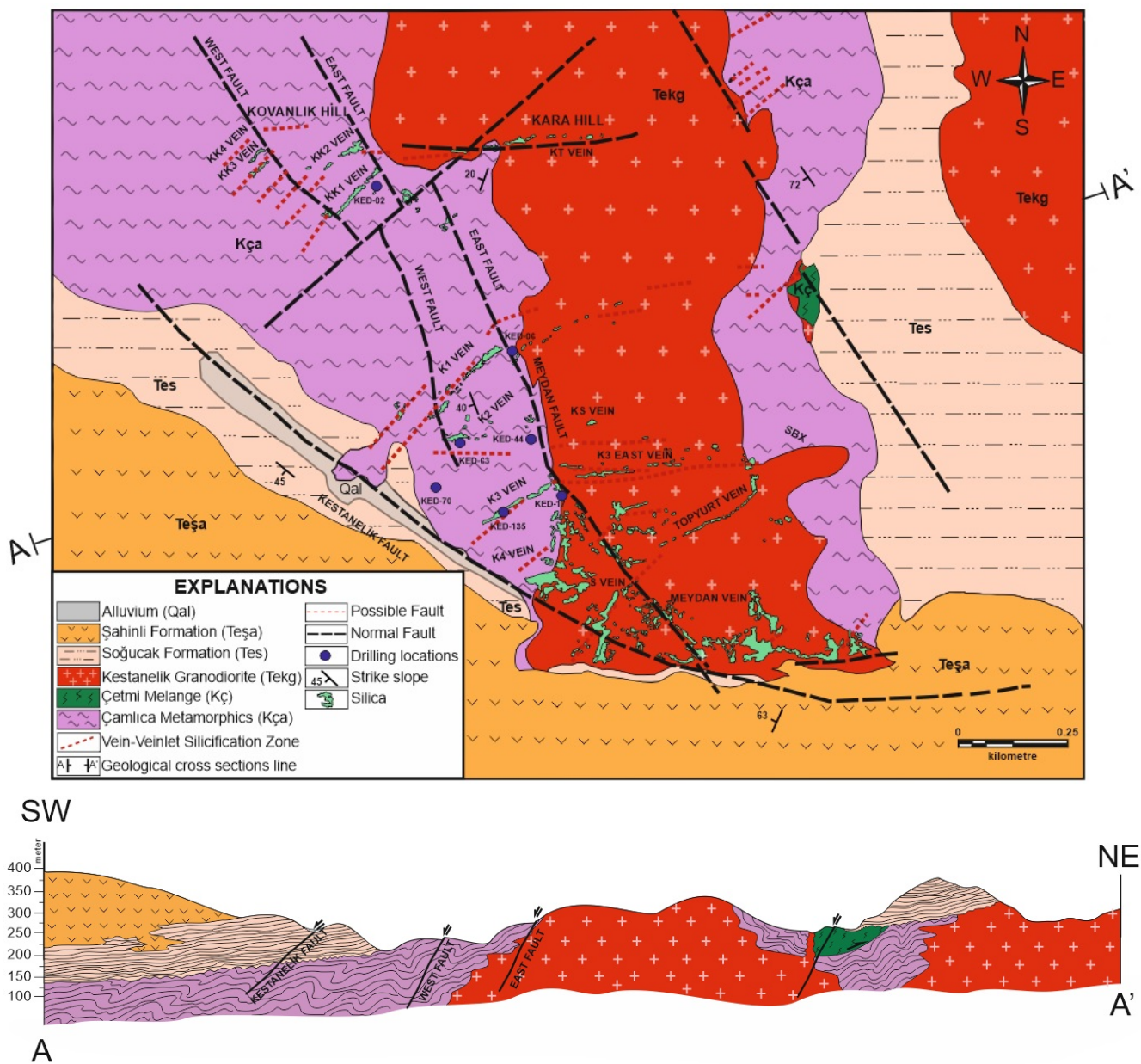


Figure 2. Geological map and cross section of the study area [22,72,73] and A–A’ geological cross-section [22].

The Çamlıca metamorphic rocks, named by the authors of [64], include sericite schist, chlorite schist, and slate–marble levels. They crop out in a wide area to the west and south of Kovanlık Hill and to the east and southeast of Kara Hill (Figure 2). The metamorphic rocks range from white, brown and gray, well-foliated, and medium-to coarse-grained mica schists at the bottom and continue with the brown-green colored phyllites upwards to the top [64,74,75]. They also include the basic rocks, marble lenses, and silicified veins. The degree of greenschist facies regional metamorphism in the clastic sedimentary rocks decreases toward the upper levels of the unit, passing into overlying schists and phyllites characterized by low-grade greenschist facies [62,75]. Based on phengite in quartz–mica schists in the Çamlıca metamorphic rocks, the ages of 65–69 Ma (Late Cretaceous) were determined using the Rb/Sr method. This result shows that Çamlıca metamorphic rocks are also affected by eclogite facies metamorphism [74]. The metamorphic rocks are intersected by Middle–Late Eocene Kestanelik granodiorite and display a tectonic connection with the Maastrichtian–Çetmi Mélange.

The intrusive mass, which was effective in the formation of the gold deposit, was emplaced as a stock into the Çamlıca metamorphic rocks [64]. This granodiorite, named the Kestanelik granodiorite [72], has been identified as quartz–feldspar–hornblende porphyry. Its N–S trend can be observed in the central part of the field (Figure 2). The granodiorite has a brecciated structure as the mine area contains many fractures due to tectonism. In the study area, the Kestanelik granodiorite intersects the Çamlıca metamorphite and the Çetmi Mélange and lies unconformably above the Soğucak Formation (Figure 2). The Laledağ granodiorite, located near the study area, was determined using the Ar/Ar method to be Middle–Late Eocene [76] (biotite  $42.08 \pm 0.09$  and hornblende  $39.21 \pm 0.11$  Ma). Because of the similarities in field observations, petrographic features, and geochemical features of the Laledağ and the Kestanelik granodiorites, the age of the Kestanelik granodiorite is assumed to be Middle-Late Eocene.

#### 4. Materials and Methods

Numerous exploration drillings were carried out in the mineralized and alteration zones in the study area, and core samples were taken from some selected drillings, including KED 02, KED 06, KED 17, KED 44, KED 70, and KED 135. A total of 31 core samples taken from these drillings consist of 11 silicified veins, 12 quartz–feldspar porphyries, and 8 quartz–mica schists (Figure 3).

To determine the mineral assemblages and alteration types of these samples, thin-section analysis for 15 samples, and X-ray diffraction (XRD)-detailed clay analysis and geochemical analysis for 31 samples were carried out. At the laboratory in the Department of Geological Engineering, Süleyman Demirel University, thin-section samples were prepared, and the mineralogical-petrographic sections were examined under an polarizing microscope equipped with a 5.1 mega-pixel camera, and images were obtained using the Image Pro Plus 5.1v image analysis system.

XRD analyses of the investigated alteration samples were carried out at the Technology Application and Research Center Laboratory–TUAM, Afyon Kocatepe University, using a Shimadzu XRD-6000 model X-ray diffractometer with a Ni filter,  $CuK\alpha$  radiation, and  $CuK\alpha$  X-ray with a 1.544 Å wavelength. For the analysis, 40 kV and 30 mA working condition values were chosen. Alteration samples were scanned at  $2^\circ/\text{min}$  and analyzed at a peak intensity of 2000 cps in the goniometer diffraction angle range of  $2\text{--}70^\circ$  ( $2\theta$ ). The mineralogy of these samples was determined by using a thorough analysis of the mineral composition of whole rocks, which were air-dried (AD) and treated with ethylene glycol (EG) at  $550^\circ\text{C}$ . For the annealed phase analysis of the samples, guide samples were prepared from the clay-sized crushed samples, and about 20–30 g of samples with a grain size of 250  $\mu\text{m}$  were used. After performing a series of standard secondary procedures on the prepared samples, artificial changes were created in the basal diffraction of clay minerals, particularly in the low  $2\theta$  angle region. The diffraction profiles of these artificial changes were examined systematically, and similar clay minerals were distinguished and defined precisely.

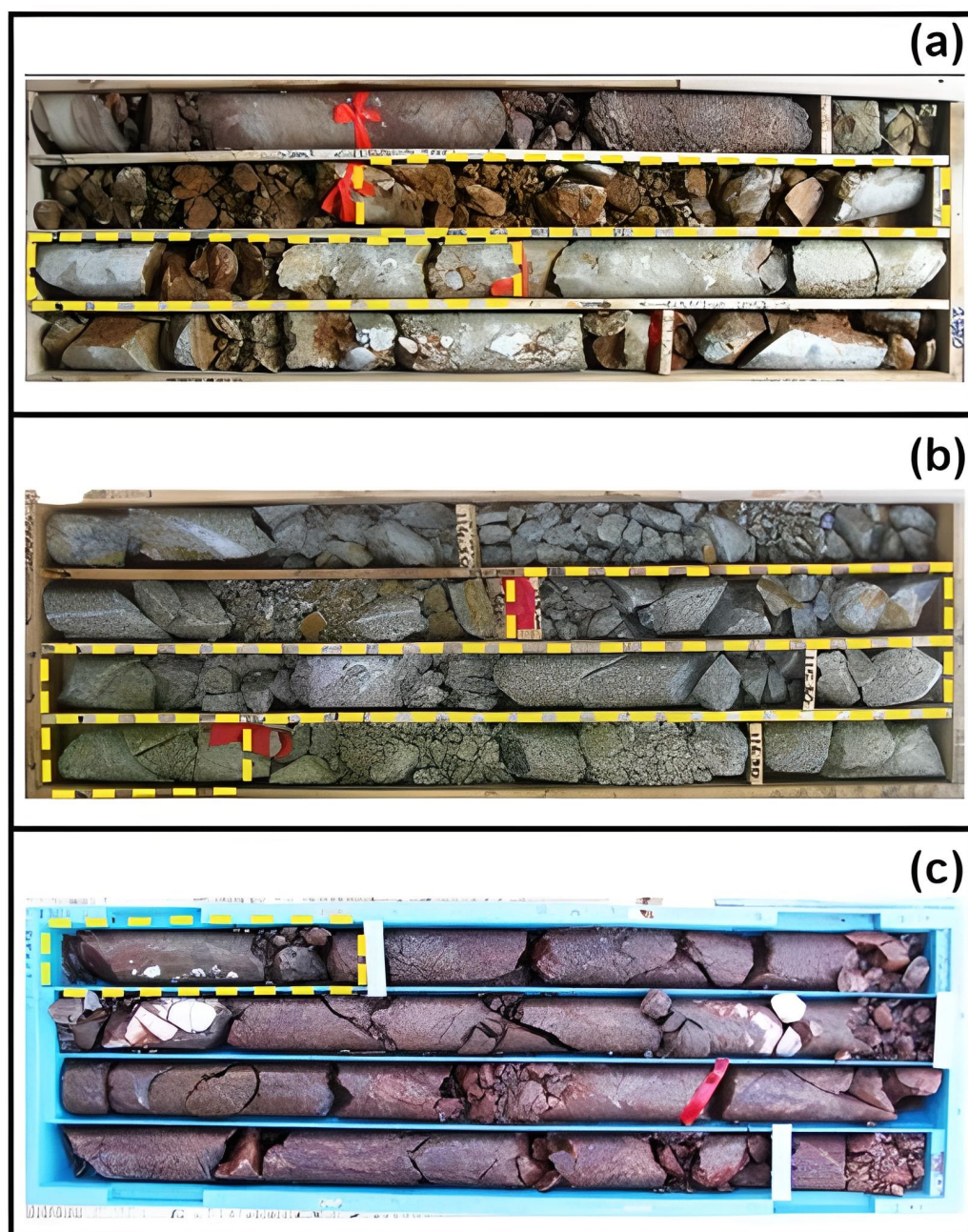


**Figure 3.** (a) Fault breccia taken from the silicified vein (KED 02–06; 26.30 m depth); (b) quartz–feldspar porphyry (KED 06–04; 115.30 m depth); (c) oxidized mica schist (KED 44–02; 3.80 m depth) [22].

Thirty-one samples were ground to 200 mesh for the chemical analyses performed at the Mineral Laboratories of Bureau Veritas (BVM), Canada. The major and minor oxides of the whole-rock samples were analyzed using emission spectrometry (ICP–OES) methods. Additionally, the trace and rare earth elements were analyzed using inductively coupled plasma-mass spectrometry (ICP–MS) after dissolving the element contents with lithium metaborate/tetraborate fusions following dilute nitric acid digestion. The detection limits are typically 0.01–0.1 wt.% for major elements, 0.01–8 ppm for trace elements, and 0.1–0.3 ppm for REEs. For evaluation of the accuracy of analytical data, the geochemical standards STD SO-18, STD DS10, STD OREAS45EA, STD GS311-1, and STD GS910-4 were used. The quality of the analyses was determined using a range of reference materials.

## 5. Results

### 5.1. Hydrothermal Alteration and Au Mineralization

Hydrothermal alteration is a common feature in epithermal mineral deposits and exhibits similar characteristics in typical epithermal deposits worldwide [8,10,11]. The hydrothermal system that formed the Au mineralization in the Kestanelik deposit occurs extensively in varying volumes and intensities, creating vein-type hydrothermal alteration zones. The deposit exhibits various alteration associations based on cutting relations, mineralogy, and distance from ore bodies. The Çamlıca quartz–mica schist rocks, Kestanelik granodiorite, and Şahinli Formation andesite–basalt rocks, which crop out in the Kestanelik gold mine area, have undergone intense alteration. Different alteration zones are clearly visible in the mine area, distinguished by their greenish-yellowish, brownish, claret, grayish, and whitish colors (Figure 4). The dominant minerals in the zones are quartz (including amethyst), hematite, limonite, goethite, opal, chalcedony, and clay minerals. The gold-bearing silicified veins in the deposit exhibit predominantly argillic, sericitic, and propylitic alteration zones, with lesser K-silicate, chloritization, and carbonation-type alteration zones observed from the inside to the outside (Figure 4).

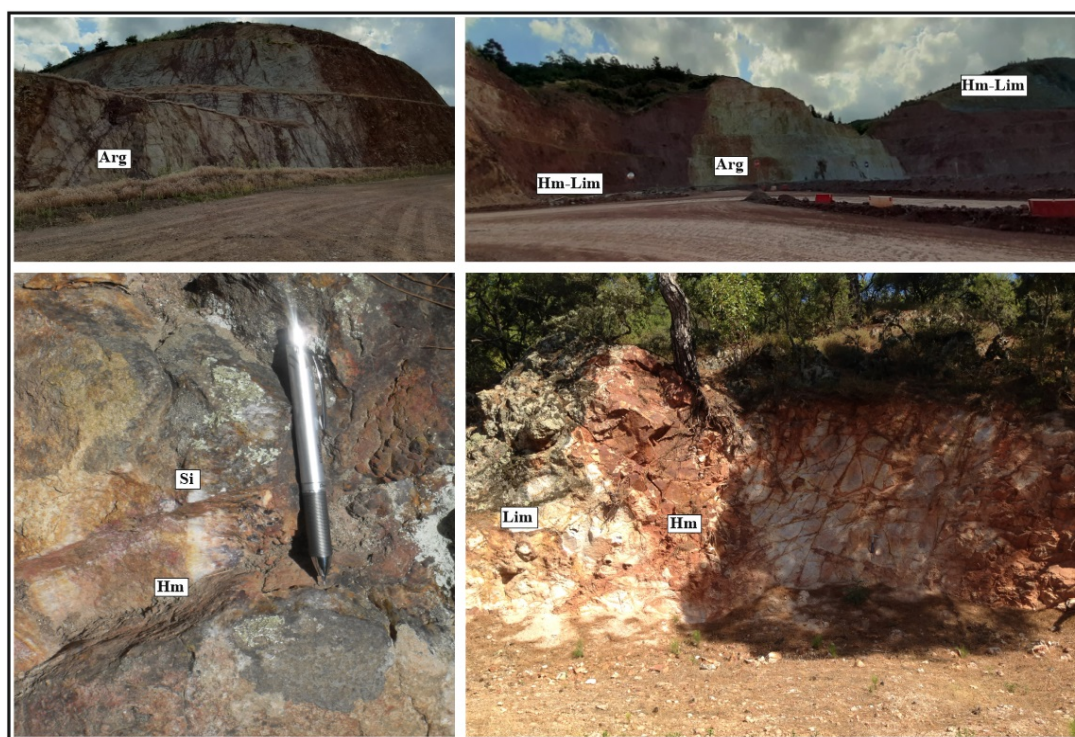


**Figure 4.** General view of hydrothermal alteration types in the study area (Arg: argillization, Si: silicification, Lim: limonitization, Hm: hematitization) [22].

The Kestanelik Au deposit is located in and around Lapseki–Şahinli village, 45 km from Çanakkale in northwestern Turkey. The Au deposit occurs in a low-sulfidation paleoenvironment [3,22,73,77–79] within the Karabiga Massif observed along the Sakarya Zone on the Biga Peninsula. The gold-bearing ore body at Kestanelik is emplaced within silicified zones of vein–stockwork veinlets that cut through the Maastrichtian–Çamlıca metamorphites and the Eocene Kestanelik granodiorite. The Kestanelik deposit’s gold mineralization consists of four primary silicified veins: Karakovan (KK1, KK2, KK3, KK4), Kara Hill (KT), Kestanelik (K1, K2, K3), and S veins. The silicified vein lengths are approximately 500 m for the Karakovan (KK1, KK2, KK3, KK4) veins, 1050 m for the Kara Hill (KT) vein, 2480 m for the Kestanelik veins (K1 vein 480 m, K2 vein 350 m, K3 vein 1650 m), and 500 m for the S vein. The deposit has an average gold grade of 2.27 g/t in the KK vein, 1.37 g/t

in the KT vein, 1.61 g/t in the K1 vein, 2.0 g/t in the K2 vein, 2.87 g/t in the K3 vein, and 2.06 g/t in the S vein [73].

The Kestanelik gold deposit is mainly accumulated in the vein–stockwork veinlets controlled by tectonic lineaments, which are represented by silicification veins and faults in the mine area. Within this area are normal faults that trend NW–SE, NE–SW, and E–W, with the Meydan and Kestanelik faults being the most significant. The ore-bearing silicified veins are intersected by NW–SE and E–W trending faults, along with NE–SW trending faults (Figure 2). Fault breccia and fault clay are present in the areas of fault deformation, and as a result of cataclastic deformation, brecciated structures are visible in the Çamlıca metamorphites, Kestanelik granodiorite, and ore-bearing silicified veins. According to [73], the Kestanelik gold deposit's host rocks and early quartz underwent cataclastic deformation and exhibit tectonic brecciation; additionally, hydrothermal fractured breccias are present, and the pre-existing vein filling displays matrix-supported chaotic breccias. Two primary permeable enrichment mechanisms responsible for the reactivation of blocked permeable pathways are co-seismic and hydraulic fracturing.

Silicified veins in the study area are typically found in the form of parallel or intersecting veins and veinlets within a silicified zone. In the silicified zones, quartz occurs in both fine and coarse crystals, while chalcedonic quartz, chalcedony, and amethyst have a fine-grained texture. The silicified zones often manifest as resistant knobs, ledges, and carapaces, with the original rock texture rarely preserved. Epithermal systems exhibit primary growth structures in the form of breccia, substitutional thrust structures, and massive, comb, crustiform–colloform, cockade, lattice-bladed, saccharoidal, moss, and banded open void fillings (Figure 5). The origin of the gold deposits at Şahinli and Tespih Dere is defined as intermediate sulfidation [3]. The deposit contains plumose quartz, comb and cockade, and matrix-supported brecciated epithermal textures. Gold and base metal minerals occur in relatively deep seated epithermal silicified veins.

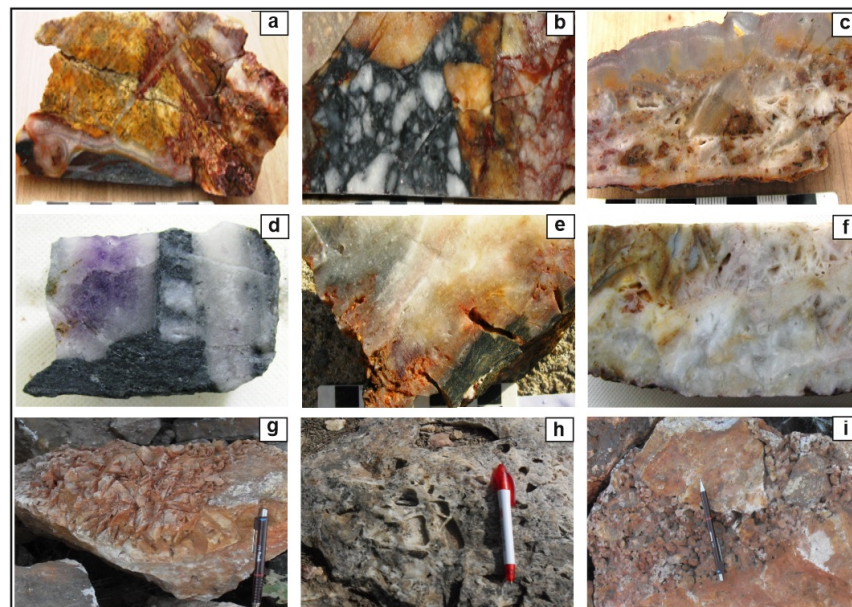


**Figure 5.** Ore structures indicating low-sulfidation epithermal systems in the study area; (a) quartz–feldspar porphyry with silica stockworks, crustiform–colloform bands with pyrite, cockade (KED 17, 22.70 m); (b) silica–breccia–quartz vein, chalcedonic, saccharoidal quartz clast in sulphide–goethite matrix (KED 06, 27.40 m); (c) silicified vein with quartz–feldspar porphyry clasts in matrix crustiform–colloform banded, cockades (KED 17, 28.40 m); (d) amethyst–crystalline quartz veinlets (KED 63, 174.50 m); (e) lattice bladed, chalcedonic, saccharoidal, moss (KED 02, 28.50 m); (f) quartz stringer, saccharoidal, crystalline, lattice bladed, hematite, limonite (KED 135, 94.40 m); (g) bladed texture in silicified zones; (h) cavity texture in silicified zones; (i) cockade texture in silicified zones [22].

## 5.2. Petrography–Mineralogy of Alteration Forms

### 5.2.1. Polarizing Microscope Investigations

The thin sections of core samples from silicified veins, Kestanelik granodiorite, and Çamlıca mica schists were examined under a polarizing microscope, and photomicrographs were taken (Figure 6a–h). Coarse-crystalline quartz typically presents a comb structure with an observed vein style for epithermal gold deposits (Figure 6a). The relationship between vein-shaped quartz, locally chloritized feldspar crystals, and a siliceous microcrystalline texture can be clearly observed in the sections (Figure 6b). Figure 6c,d shows cataclastic-textured and coarse-grained quartz and muscovite, with lesser amounts of biotite and opaque minerals. Another examined thin-section sample suggests a rhyolitic composition, with coarse crystalline quartz and locally corroded opaque minerals present (Figure 6f). In certain sections of the area, feldspars and amphiboles underwent chloritization, while micas experienced sericitization in some areas (Figure 6e–h).

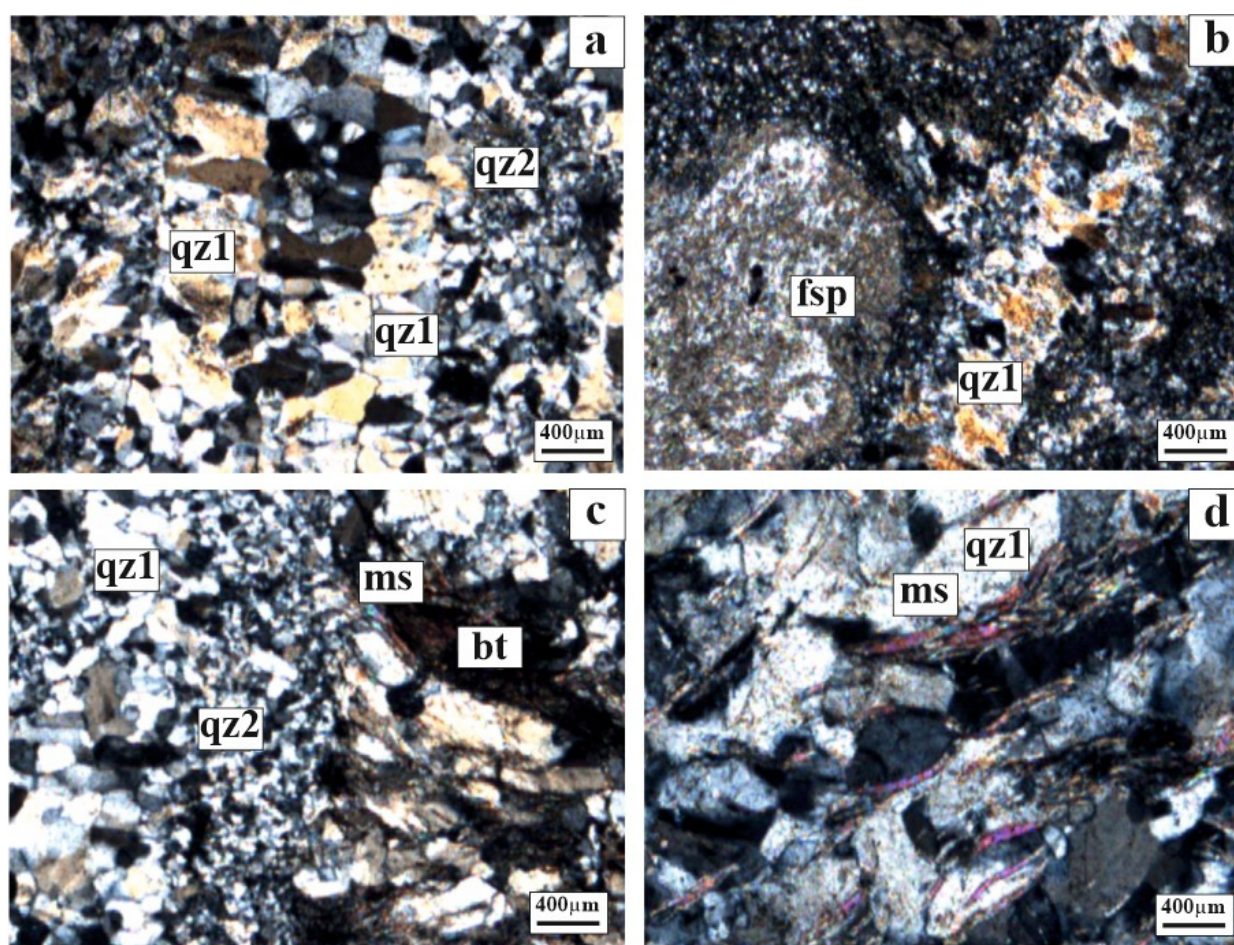
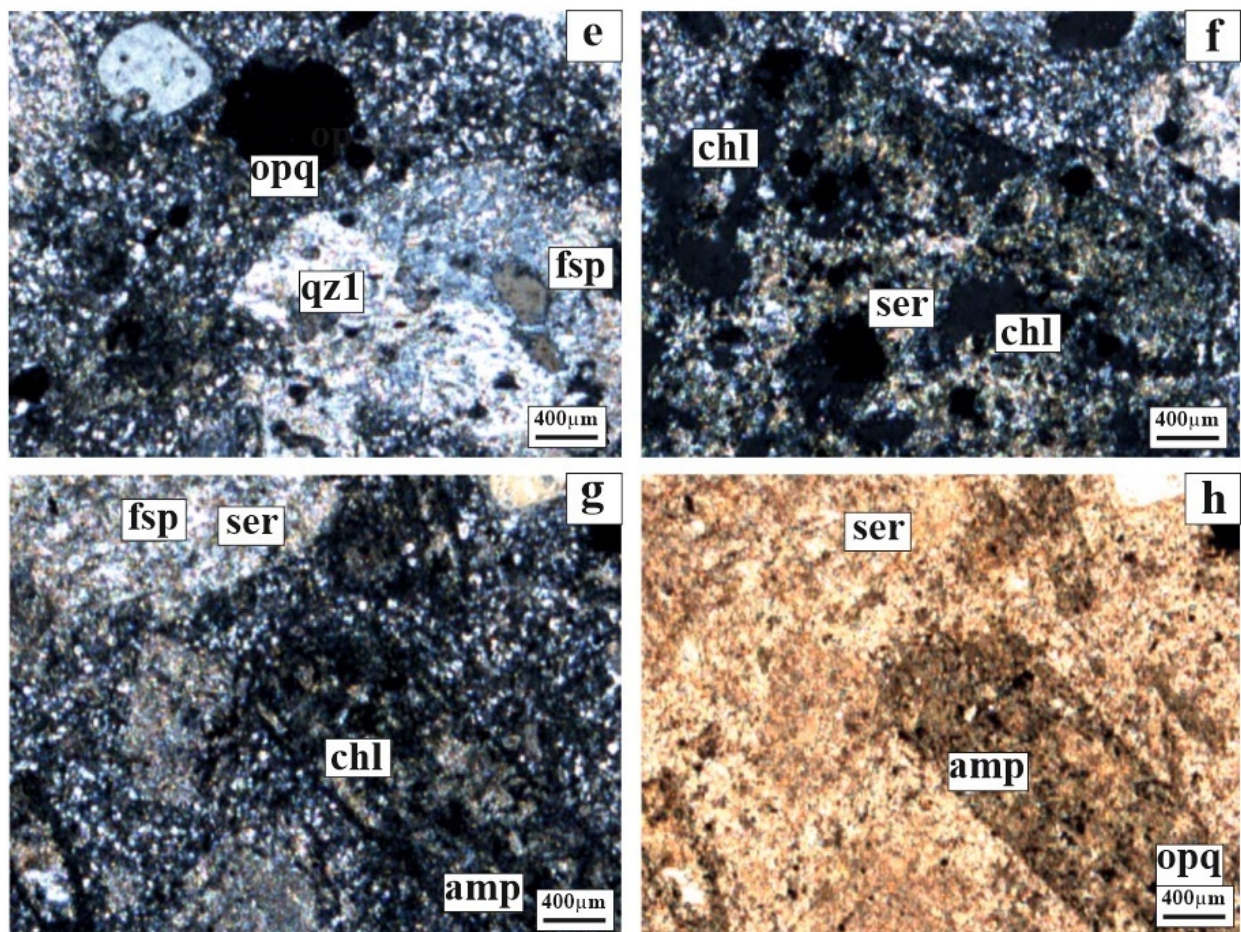


Figure 6. Cont.



**Figure 6.** Photomicrographs in cross polarized and plane polarized light of various rock samples; (a) quartz (qz1, qz2) with two stage and comb structure; (b) feldspar (fsp) and vein quartz (qz1); (c) the relationship between quartz (qz1, qz2) and muscovite (ms)–biotite (bt); (d) coarse crystalline quartz (qz1) and muscovite (ms); (e) coarse-grained quartz (qz1), feldspar (fsp) and euhedral opaque mineral (opq); (f) chloritization (chl) and sericitization (ser); (g,h) feldspar (fsp), amphibole (amp), sericitization (ser) and chloritization (chl) [22].

### 5.2.2. X-ray Diffraction-Mineralogy of Alteration

X-ray diffraction (XRD) clay analysis was conducted on core samples taken from the Kestanelik gold ore deposit, specifically from silicified vein, altered quartz–feldspar porphyry, and quartz–mica schist rocks. The results of the analysis and representative patterns of samples taken from the silicified vein, quartz–feldspar porphyry, and quartz–mica schist can be found in Figure 7. The mineral compositions of these altered rocks are listed separately in Table 1. All of the samples were mainly composed of illite–mica and quartz. Minor amounts of calcite, dolomite, feldspar, and hornblende are also present. Smectite, chlorite, and kaolinite are alteration minerals (Figure 7). Smectite minerals are characterized by  $d(001)$  values of 12.98–14.29 Å in air-dried clay mineral samples (AD). In samples treated with ethylene glycol (EG), the  $d(001)$  surfaces expand to the range 16.90–17.45 Å. However, at a temperature of 550 °C, the samples' surface  $d(001)$  shrinks to the range 9.98–10.06 Å (Figure 7). Chlorite minerals are characterized by surface reflections at 12.23–12.40  $d(001)$ , 7.11–7.18  $d(002)$ , and 3.57  $d(003)$ . They can be distinguished from smectite and kaolinite by observing that their characteristic peaks remain unchanged after ethylene glycol and heat treatments. Upon heating to 550 °C, the reflection of kaolinite's (001) plane at 7.11–7.18  $d$ -spacing disappears due to the dehydroxylation process [80].

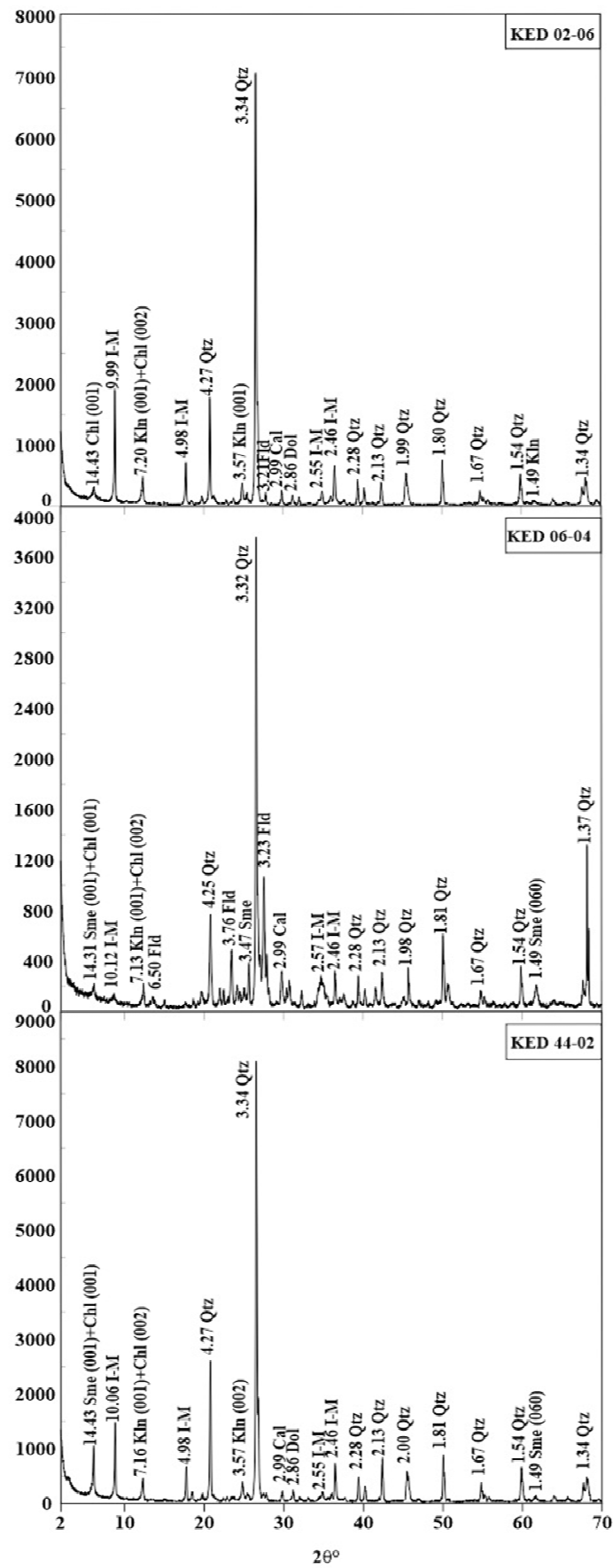
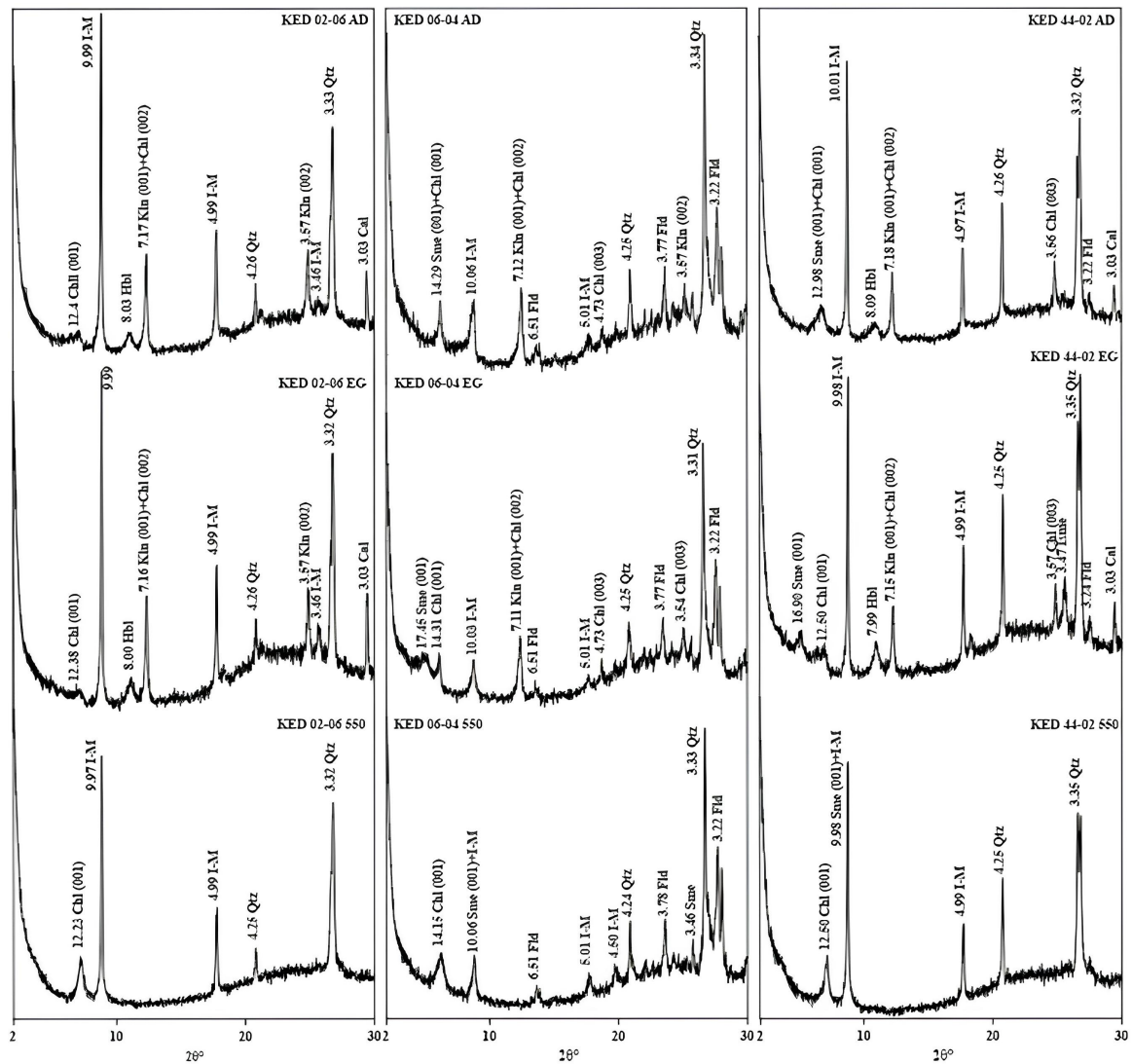


Figure 7. Cont.



**Figure 7.** Representative XRD patterns of bulk samples and clay fraction of the samples from silicified veins (KED 02-06), quartz+feldspar porphyry (KED 06-04), and quartz-mica schist (KED 44-02), AD: air dried, EG: ethylene glycolated, (550): heated at 550 °C [22]. Abbreviations: Qtz: quartz, I-M: illite-mica, Kln: kaolinite, Fld: feldspar, Chl: chlorite, Kln+Chl: kaolinite+chlorite, Sme+Chl: smectite+chlorite, Sme: smectite, Sme+I-M: smectite+illite-mica, Cal: calcite, Dol: dolomite, Hbl: hornblende.

**Table 1.** Mineral abundances of core alteration samples in the study area [22].

Sample Number	Sample Type	Qtz	I-M	Sme+I-M	Kln	Fld	Chl	Kln+Chl	Sme+Chl	Sme	Cal	Dol	Hm	Alu	Hbl
KED02-02	SV	16	3	0	2	0	0	0	0	0	2	0	0	0	0
KED02-06	SV	16	10	0	3	0	6	0	0	2	3	1	0	0	1
KED02-07	SV	16	6	0	4	0	0	0	0	0	1	0	0	0	0
KED02-13	SV	17	0	0	0	0	0	0	0	0	1	0	0	0	0
KED17-08	SV	15	0	0	2	0	0	0	0	0	3	0	0	0	0
KED63-02	SV	17	8	1	2	4	11	2	1	1	0	0	0	0	0
KED63-03	SV	8	9	0	2	1	10	2	0	0	3	1	0	0	0
KED63-05	SV	17	8	1	5	1	0	0	0	4	2	1	0	0	0
KED63-09	SV	15	3	0	0	0	0	0	0	0	2	0	0	0	0
KED63-10	SV	17	8	0	6	1	0	0	0	0	2	0	1	0	0

Table 1. Cont.

Sample Number	Sample Type	Qtz	I-M	Sme+I-M	Kln	Fld	Chl	Kln+Chl	Sme+Chl	Sme	Cal	Dol	Hm	Alu	Hbl
KED63-11	SV	16	8	0	2	1	9	2	0	0	4	1	0	0	0
KED06-03	QFP	15	0	0	2	5	7	0	0	3	2	1	1	0	0
KED06-04	QFP	16	7	0	1	13	9	0	0	4	3	1	1	0	0
KED06-05	QFP	14	6	0	2	11	6	0	0	5	3	1	1	0	0
KED06-06	QFP	15	6	1	1	12	6	0	1	9	1	1	0	0	0
KED06-07	QFP	18	3	0	1	11	5	0	1	7	2	1	0	0	0
KED06-08	QFP	13	4	0	2	9	4	0	0	3	0	0	0	0	0
KED06-10	QFP	15	4	0	1	11	9	0	0	4	1	1	0	0	0
KED17-01	QFP	11	7	0	0	9	0	0	0	3	1	0	1	0	0
KED17-02	QFP	12	6	0	0	10	0	0	0	0	0	0	0	0	0
KED17-06	QFP	16	0	0	0	3	0	0	0	0	0	0	0	0	0
KED17-07	QFP	15	3	0	0	8	0	0	0	0	2	0	0	0	0
KED135-3	QFP	17	7	1	4	12	0	0	0	9	3	0	1	2	0
KED02-05	QMS	16	8	0	2	0	0	0	0	0	3	0	0	0	0
KED02-11	QMS	16	8	0	2	0	0	0	0	0	2	0	0	0	0
KED06-11	QMS	14	9	0	6	8	0	0	0	2	3	0	0	0	0
KED44-02	QMS	16	6	3	2	3	8	0	1	2	2	0	0	0	0
KED44-03	QMS	17	9	0	0	1	7	0	0	0	3	1	0	0	0
KED44-12	QMS	15	2	0	0	5	13	0	0	0	3	1	1	0	0
KED70-01	QMS	18	0	0	2	0	0	0	0	0	2	0	0	0	0
KED70-02	QMS	15	9	0	0	2	12	0	0	0	4	1	0	0	0

Abbreviations: SV: silicified vein, QMS: quartz–mica schist, QFP: quartz–feldspar porphyry, Qtz: quartz, I-M: illite-mica, Sme+I-M: smectite+illite-mica, Kln: kaolinite, Fld: feldspar, Chl: chlorite, Kln+Chl: kaolinite+chlorite, Sme+Chl: smectite+chlorite, Sme: smectite, Cal: calcite, Dol: dolomite, Hm: hematite, Alu: alunite, Hbl: hornblende.

### 5.3. Geochemistry

#### 5.3.1. Petrogenic Elements

Thirty-one samples were taken from silicified vein, quartz–feldspar porphyry, and quartz–mica schist. The samples were collected from 7 drillings obtained in the drilling cores in the Kestanelik gold mine area. Table A1 presents the results of the analysis of major and minor oxides and trace and rare earth elements in the alteration samples.

The major oxide contents of silicified vein samples reveal the following ranges: 57.74–98.02 wt.% SiO<sub>2</sub>, 0.50–14.33 wt.% Al<sub>2</sub>O<sub>3</sub>, 0.60–8.03 wt.% Fe<sub>2</sub>O<sub>3</sub>, 0.03–3.59 wt.% K<sub>2</sub>O, and 0.04–4.13 wt.% MgO, according to the results. The altered quartz–feldspar porphyry samples have values that range as follows: 64.79–89.52 wt.% SiO<sub>2</sub>, 3.34–16.61 wt.% Al<sub>2</sub>O<sub>3</sub>, 2.10–3.61 wt.% Fe<sub>2</sub>O<sub>3</sub>, 0.38–1.51 wt.% MgO, 0.07–8.00 wt.% Na<sub>2</sub>O, and 2.06–9.21 wt.% K<sub>2</sub>O. The altered quartz–mica schist samples indicate the following elemental content ranges: 52.92–95.78 wt.% SiO<sub>2</sub>, 1.19–14.85 wt.% Al<sub>2</sub>O<sub>3</sub>, 0.65–14.06 wt.% Fe<sub>2</sub>O<sub>3</sub>, 0.09–4.78 wt.% MgO, 0.01–3.61 wt.% K<sub>2</sub>O, and 0.01–1.63 wt.% TiO<sub>2</sub>. Other major oxide concentrations are below 1% and insignificant (Table A1). When comparing all three rock types in terms of major oxides, SiO<sub>2</sub> in the silicified vein; Al<sub>2</sub>O<sub>3</sub>, K<sub>2</sub>O, and Na<sub>2</sub>O in the quartz–feldspar porphyry; and Fe<sub>2</sub>O<sub>3</sub>, MgO, and TiO<sub>2</sub> in the quartz–mica schist shows higher values.

Au, Ag, Sb, As, Hg, Bi, Se, Te, and base metals (Pb, Zn, Cu) are trace elements commonly found in epithermal gold deposits. In the zone of silicification alteration, Sb, Hg, and Bi elements are present, along with Au and Ag. These elements are also accompanied by Cu, Mo, and Te, which are found in propylitized zones. Manganese and zinc, which characterize the propylitization areas, are accompanied by Cu, Mo, and Te [81]. The surface or shallower levels of the metal zoning contain Tl, Hg, As, and Sb, followed by Au and Ag. The Ag/Au ratio increases with depth, and the mineralization ends in a deep zone characterized by base metal (Cu, Pb, Zn) enrichment containing Cd and Se [82–84]. The

trace element contents in different rock types associated with gold mineralization were compared. The silicified veins were found to have slightly higher average concentrations of Au (784 ppb), Sb (40.1 ppm), and Pb (54.1 ppm). The quartz–mica schist samples show slightly higher average levels of Ag (1.8 ppm), As (158.6 ppm), Cu (28.9 ppm), and Zn (62 ppm) compared to the reference values presented in Table A1. The Kestanelik field; samples show an average Au grade of 2.27 g/t in the KK vein samples, 2.0 g/t in the K2 vein samples, and 2.87 g/t in the K3 vein samples [73]. In contrast, the average gold content of the core samples taken from the silicified vein (KK1, K2, K3) analyzed in this study was determined to be less than 1 g/t.

### 5.3.2. Rare Earth Elements

Rare earth elements (REEs), particularly those found in K-silicate, sericitic, argillic, and propylitic alteration types, may be reactivated during the alteration process [6,85–88]. Figure 8 shows separate plots of chondrite-normalized [85] REE models for the samples of silicified vein, quartz–feldspar porphyry, and quartz–mica schist. The ( $\Sigma$ REE) values of the mineralized epithermal silicified vein and quartz–mica schist rock samples are depleted and similar (65.95 and 63.24 ppm). However, an increase in  $\Sigma$ REE content is observed from slightly altered porphyries to silicified veins.

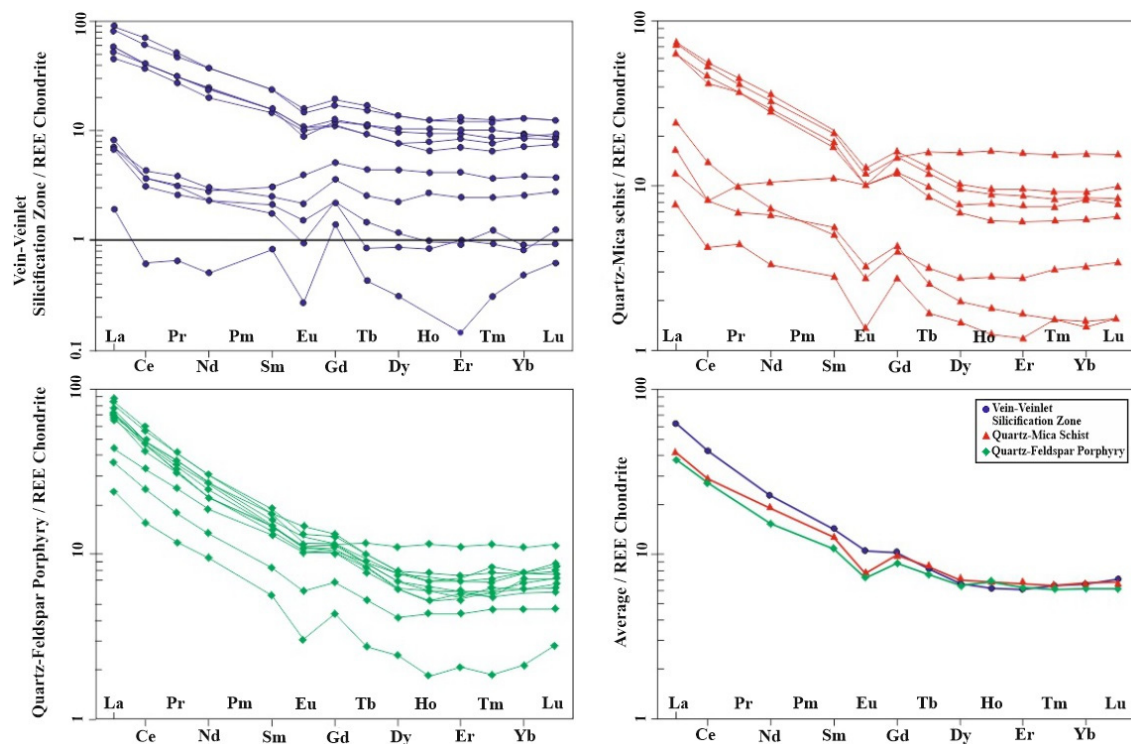


**Figure 8.** Comparison of chondrite-normalized REE patterns of variable altered rock samples [22,85].

In contrast, the quartz–feldspar porphyry rock samples have the highest  $\Sigma$ REE values (81.06 ppm) and are enriched in total REE contents. However, the REE patterns in rocks indicating LREE enrichment show similar trends, as the average LREE/HREE ratio is 2.85, 4.04, and 3.12 for silicified vein, quartz–feldspar porphyry, and quartz–mica schist, respectively (Table 2). The concentration of REEs in all rocks tends to decrease with increasing hydrothermal alteration intensity (Figure 8). The mean (La/Yb)<sub>n</sub> and (La/Sm)<sub>n</sub> values of samples from silicified vein, altered quartz–feldspar porphyry, and quartz–mica schist are 5.87–3.30, 9.84–4.41, and 7.49–3.21, respectively. Table 2 shows that the (La/Yb)<sub>n</sub> and (La/Sm)<sub>n</sub> values of quartz–feldspar porphyry are slightly higher than the others.

**Table 2.** REE values of variable altered rocks.

Sample Type	Mean Eu/Eu*	La/Yb	La/Sm	LREE/HREE	ΣREE
Silicified vein	0.72	5.87	3.30	2.85	65.95
Quartz–feldspar porphyry	0.82	9.84	4.41	4.04	81.06
Quartz–mica schist	0.66	7.49	3.21	3.12	63.24

The REE distribution patterns of epithermal silicified vein, quartz–feldspar porphyry, and quartz–mica schist samples, normalized to chondrite, exhibit negative Eu anomalies. The mean Eu/Eu\* values for these samples are 0.72, 0.82, and 0.66, respectively. Negative Eu anomalies indicate the presence of Eu<sup>2+</sup>, while positive Eu anomalies suggest the presence of Eu<sup>3+</sup>. As Eu<sup>2+</sup> has nearly the same radius as Ca<sup>2+</sup>, it naturally substitutes into the Ca site [89]. These negative Eu<sup>2+</sup> anomalies indicate low oxygen fugacity during plagioclase crystallization from the magma, followed by divalent mobilization.

The correlation between ΣREE and P<sub>2</sub>O<sub>5</sub>, Al<sub>2</sub>O<sub>3</sub>, TiO<sub>2</sub>, and K<sub>2</sub>O values suggests an increase in REE-bearing minerals in the altered rocks (Figure 9).

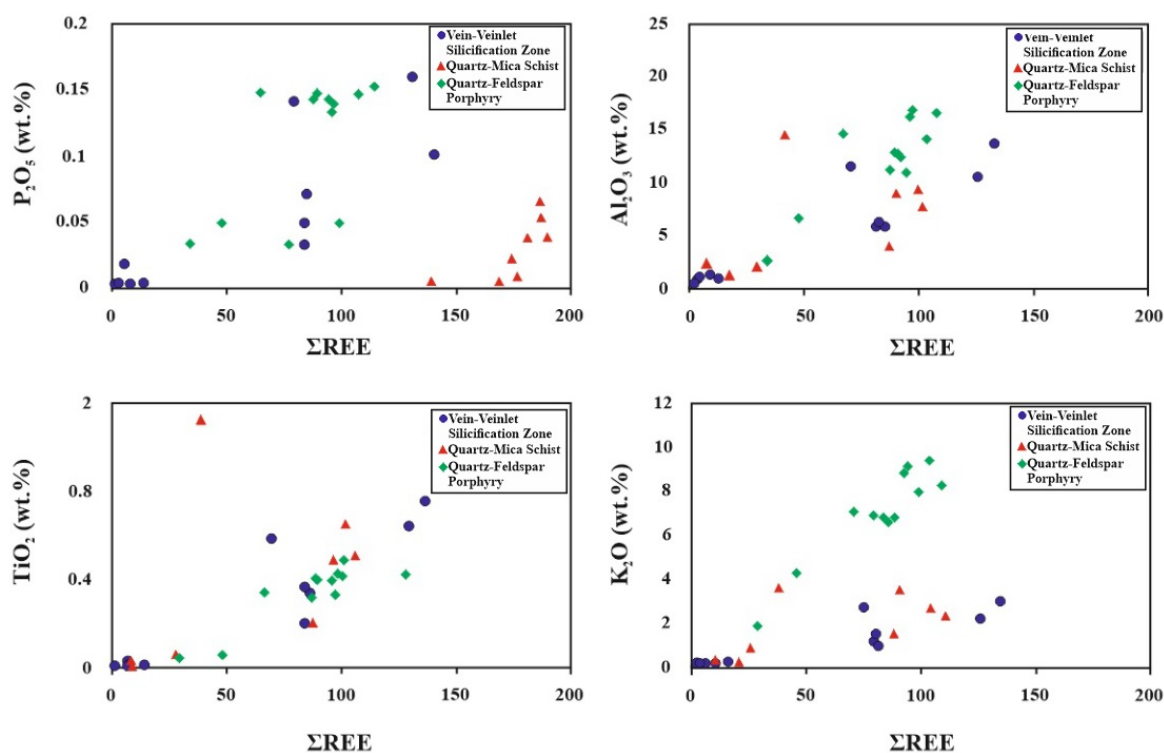


**Figure 9.** Distribution graphs showing relation between ΣREE and P<sub>2</sub>O<sub>5</sub>, Al<sub>2</sub>O<sub>3</sub>, TiO<sub>2</sub>, and K<sub>2</sub>O for silicified vein, altered quartz–feldspar porphyry and quartz–mica schist samples in the study area [22].

#### 5.4. Hydrothermal Alteration Indices

To determine the alteration in silicified vein, quartz–feldspar porphyry, and quartz–mica schist samples in the study area, we used the Ishikawa alteration index (AI), chlorite–carbonate–pyrite index (CCPI), sericite index (SI), and chemical alteration index (CIA). The Ishikawa alteration index (AI), as described by [36], is one of the most widely used indices for determining hydrothermal alteration. This index calculates the ratio of the basic rock-forming elements gained during the chlorite and sericite exchange (MgO + K<sub>2</sub>O) to the elements lost and gained (Na<sub>2</sub>O + CaO + MgO + K<sub>2</sub>O). The chlorite–carbonate–pyrite index is calculated as  $CCPI = 100 \times \text{MgO} + \text{FeO} / (\text{MgO} + \text{FeO} + \text{Na}_2\text{O} + \text{K}_2\text{O})$  [47] and is used as the second index for determining alteration types. The rock's FeO is the total Fe

content ( $\text{FeO} + \text{Fe}_2\text{O}_3$ ). The index measures the increase in MgO and FeO resulting from the development of Mg-Fe chlorite in igneous rock. This process often replaces albite, K feldspar, or sericite, leading to the loss of  $\text{Na}_2\text{O}$  and  $\text{K}_2\text{O}$  [47].

In the study area, the alteration index (AI) values range from 54.17 to 95.90, while the chlorite–carbonate–pyrite index values range from 57.67 to 98.08 in geochemical studies. The Ishikawa alteration index and chlorite–carbonate–pyrite index diagrams indicate the samples' hydrothermal decomposition and alteration trend in the following order of abundance: Chlorite–pyrite, sericite–chlorite–pyrite, chlorite–pyrite–sericite, and chlorite–carbonate. Figure 10a shows the areas of the diagram where the alteration samples fall. All rock samples exhibit hydrothermal alteration types that are mainly argillic- and chlorite type. Propylitic alteration is only present in the vein–veinlet silicification zone (Figure 10b).

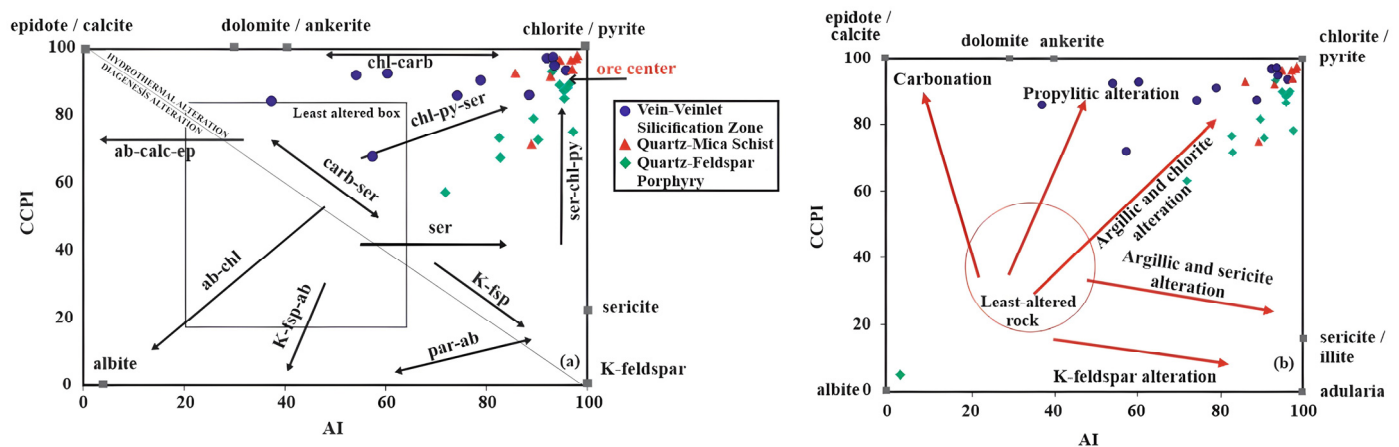


**Figure 10.** (a) Ishikawa alteration index (AI) and (b) chlorite–carbonate–pyrite index (CCPI) trend diagrams [47]. Abbreviations: chl-carb: chlorite-carbonate, chl-py-ser: chlorite-pyrite-sericite, ser-chl-py: sericite-chlorite-pyrite, carb-ser: carbonate-sericite, K-fsp: K-feldspar, ser: sericite, ab-calc-ep: albite-calcite-epidote, ab-chl: albite-chlorite, K-fsp-ab: K-feldspar-albite, par-ab: paragonitic-sericite-albite.

The alteration samples from the study area show a dominant presence of chlorite–sericite and sericite alteration minerals, with fewer samples falling in the adularia–sericite mineral assemblage field (Figure 11). The relationship between the  $\text{Na}_2\text{O}$ ,  $\text{K}_2\text{O}$ ,  $\text{Al}_2\text{O}_3$ ,  $\text{CaO}$ ,  $\text{MgO}$ , and  $\text{FeO}$  values of the samples and the Ishikawa alteration index was also analyzed. This paragenesis indicates the existence of argillic, sericitic, and propylitic alteration types that are characteristic of epithermal deposits with low sulfidation. As a result of the increase in the alteration index towards the ore veins, the potassium and aluminum contents, as well as the sericite–clay minerals, increased in quartz–mica schist rocks compared to other rock groups due to K–Al metasomatism. Conversely, the sodium, calcium, magnesium, and iron contents decrease (Figure 11).

The efficiency of sericitization alteration in rocks was determined by calculating the sericitization index (SI), defined as  $\text{SI} = \text{K}_2\text{O}/(\text{K}_2\text{O} + \text{Na}_2\text{O})$  [38]. Plotting the SI values versus  $(\text{K}_2\text{O} + \text{Na}_2\text{O})$  values on a diagram shows that all the alteration samples from the study area fall within the hydrothermal alteration area. SI index values of most of the vein–veinlet silicified samples and quartz–mica schist samples, as well as all samples of quartz–feldspar porphyry in the hydrothermal alteration area, are above 1.0 and exhibit a linear relationship (Figure 12a). The SI values versus the  $\text{CaO}$  values increase in quartz–feldspar porphyry, but there is an increase and decrease in the vein–veinlet silicified rocks and quartz–mica schists, indicating weak carbonation (Figure 12b).

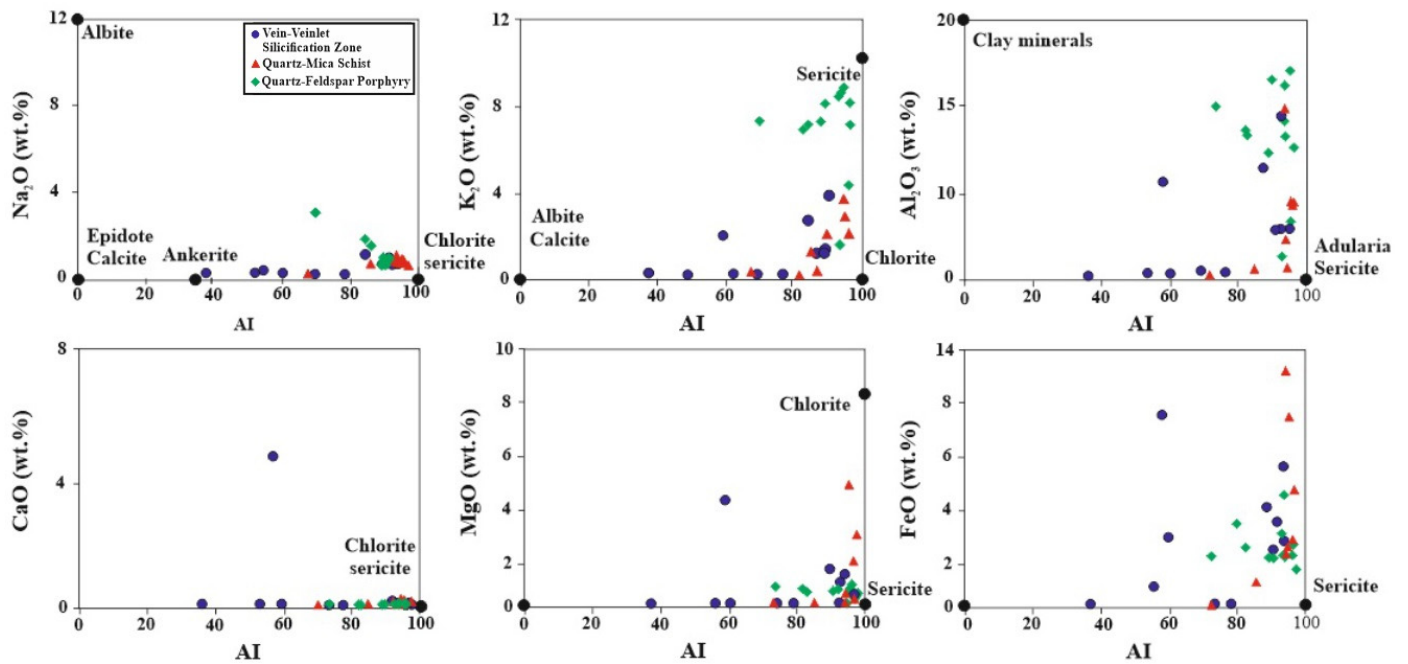


Figure 11. The relationship diagram between the alteration index (AI) and mainly major oxide contents [47].

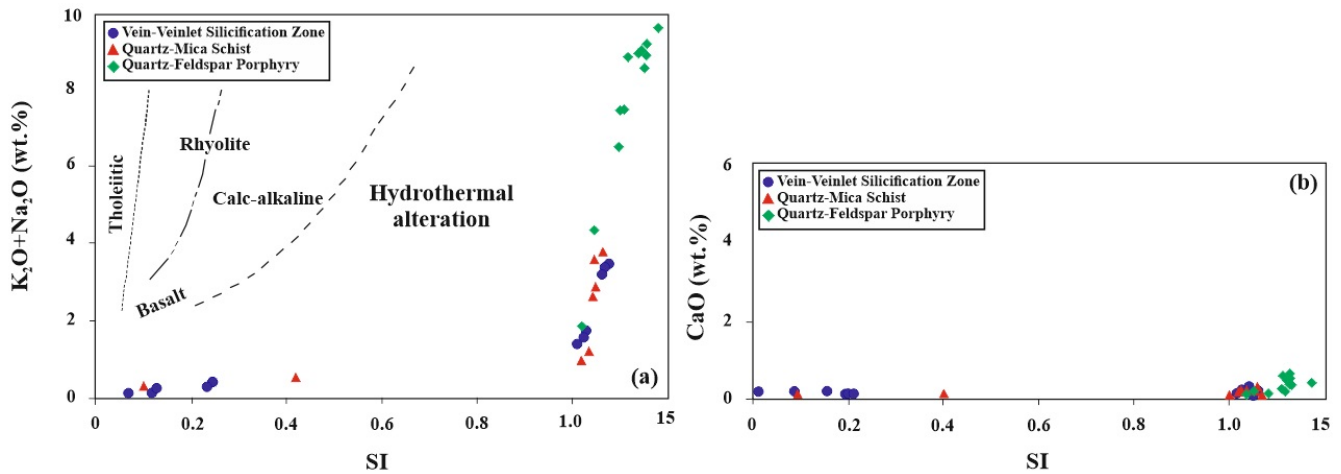
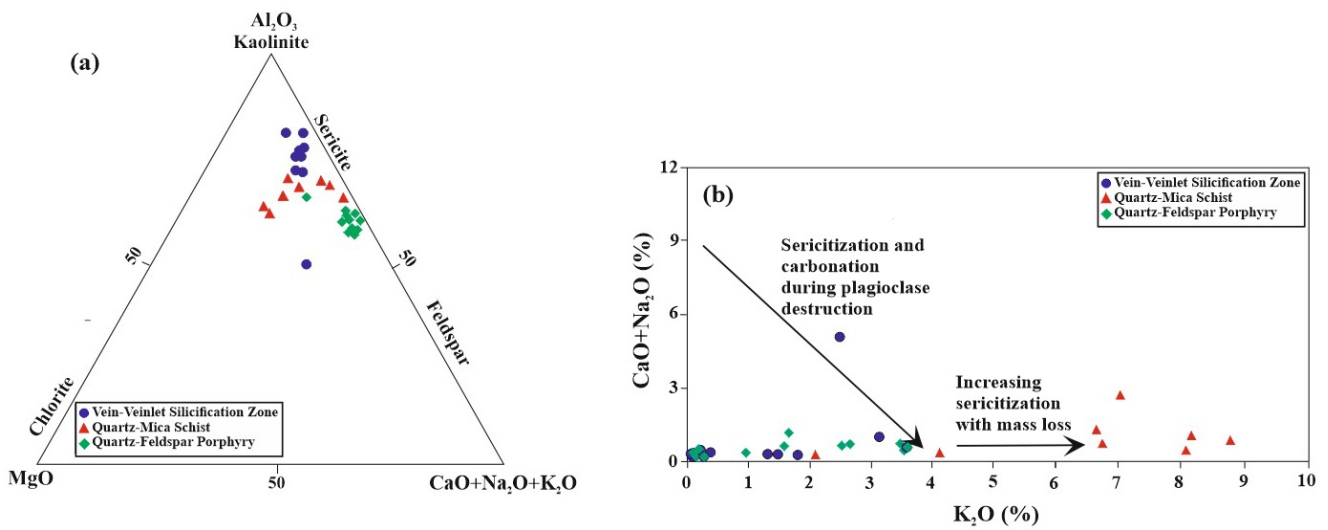


Figure 12. (a) SI versus (K<sub>2</sub>O + Na<sub>2</sub>O) and (b) SI versus CaO distribution diagrams of altered samples in the study area [39].

The triangular diagram for Al<sub>2</sub>O<sub>3</sub>–MgO–(CaO + Na<sub>2</sub>O + K<sub>2</sub>O) and the K<sub>2</sub>O versus CaO + Na<sub>2</sub>O variation diagram clearly show evidence of sericitization in all rocks due to mica and/or plagioclase alteration (Figure 13a,b). In the graph of K<sub>2</sub>O versus CaO + Na<sub>2</sub>O, CaO + Na<sub>2</sub>O values decrease in the vein–veinlet silicification zone and quartz–feldspar porphyry, while K<sub>2</sub>O values increase in the quartz–mica schist samples. This suggests that sericite formation began with the decomposition of mica (Figure 13b). According to the authors of [89], this is due to the alkali change in the sericitization process and the addition of K from hydrothermal fluids.



**Figure 13.** Distribution of samples in the study area in (a)  $Al_2O_3$ – $MgO$ –( $CaO + Na_2O + K_2O$ ) triangular diagram [90], (b)  $K_2O$  versus  $CaO + Na_2O$  diagram [89].

The chemical weathering index (CIA) and the  $Al_2O_3$ –( $CaO + Na_2O$ )– $K_2O$  (A–CN–K) triangle diagram [37] were used to assess alteration trends. The diagram shows that the vein–veinlet silicification zone in the study area contains mostly illite and smectite; quartz–feldspar porphyries with muscovite, biotite, and smectite; and quartz–mica schists with illite, muscovite, biotite, and smectite (Figure 14a). Based on the  $Al_2O_3$ –( $Na_2O + K_2O$ )–( $Fe_2O_3 + MgO$ )– $K_2O$  triple diagram [18], the vein–veinlet silicification zone and quartz–mica schist samples are classified as falling within the potassium silicate (K-silicate), propylitic, and sericitic categories. The quartz–feldspar porphyry samples, however, are mostly classified as falling within the propylitic category and, to a lesser extent, the potassium silicate category (Figure 14b).

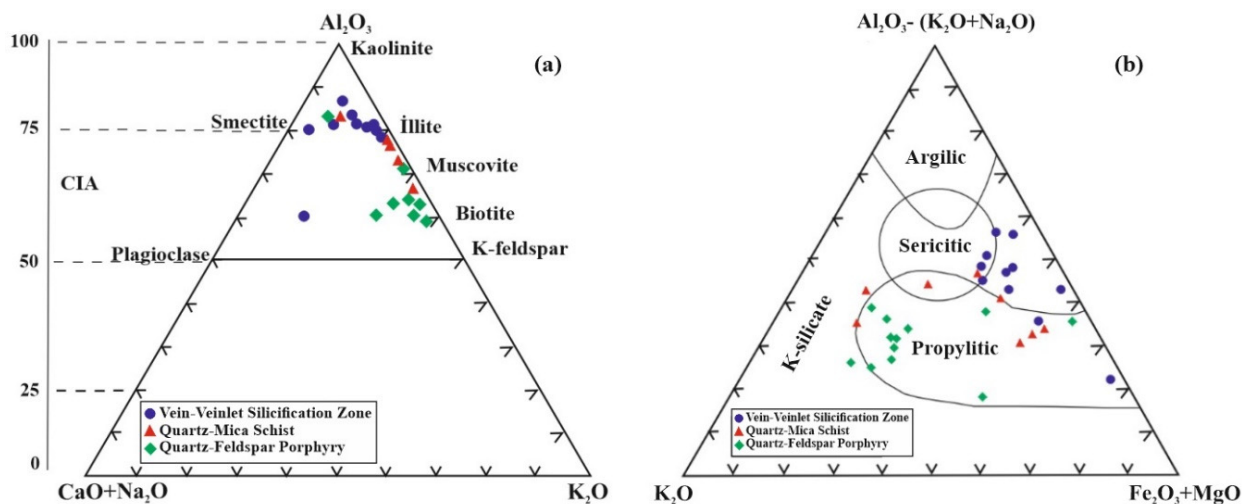


**Figure 14.** (a) Distribution of samples in ACNK diagram and classification according to CIA (chemical alteration index) value [37], (b)  $Al_2O_3$ –( $Na_2O + K_2O$ )– $Fe_2O_3 + MgO$ – $K_2O$  ternary diagram [18].

### 5.5. Molar Ratio and Mass Gain/Loss

Molar ratio graphs are useful in calculating the mass loss and gain resulting from alteration in magmatic rocks [40–42] and mineral deposits, particularly in relation to large hydrothermal systems [51–54]. Several methods have been used to calculate mass loss and gain in ore deposits [22,35,46,48]. The process of mass exchange via hydrothermal alteration minerals is also explained. These methods offer a graphical means for evaluating

the extent of K and Ca-metasomatism, as well as Ca and Na depletion, in altered rocks. The methods also provide comparisons for geochemical assessment of mineralogical tendency that is focused on epithermal ore bodies and the compositions of hydrothermal minerals and altered rocks contained therein.

The resulting data were used to plot the  $(2Ca + Na + K)/Al$  and  $K/Al$  molar element ratios, as shown in Figure 15. The process of mass exchange via hydrothermal alteration minerals is also explained. In the study area, the quartz–feldspar porphyry samples fall into the category of feldspar composition and biotite mixes on the left side of the vertical line, where the  $2Ca + Na + K/Al$  value is 1.0 on the  $x$ -axis. This suggests the presence of intense alteration, with an increase in K-metasomatism and a decrease in Ca and/or Na metasomatism. The vein–veinlet silicification zone and quartz–mica schist samples fall into the K-mica area. These data indicate the presence of sericitic and argillic alteration types. In the study area, a sample from the vein–veinlet silicification zone and a sample from quartz–feldspar porphyry fall within the range to the right of the vertical line on the  $x$ -axis, where the  $2Ca + Na + K/Al$  value is 1.0 (Figure 15). This suggests an increase in Na, Ca, and K in these samples, with propylitic alteration in the quartz–feldspar porphyry and silicic alteration in the vein–veinlet silica zone.

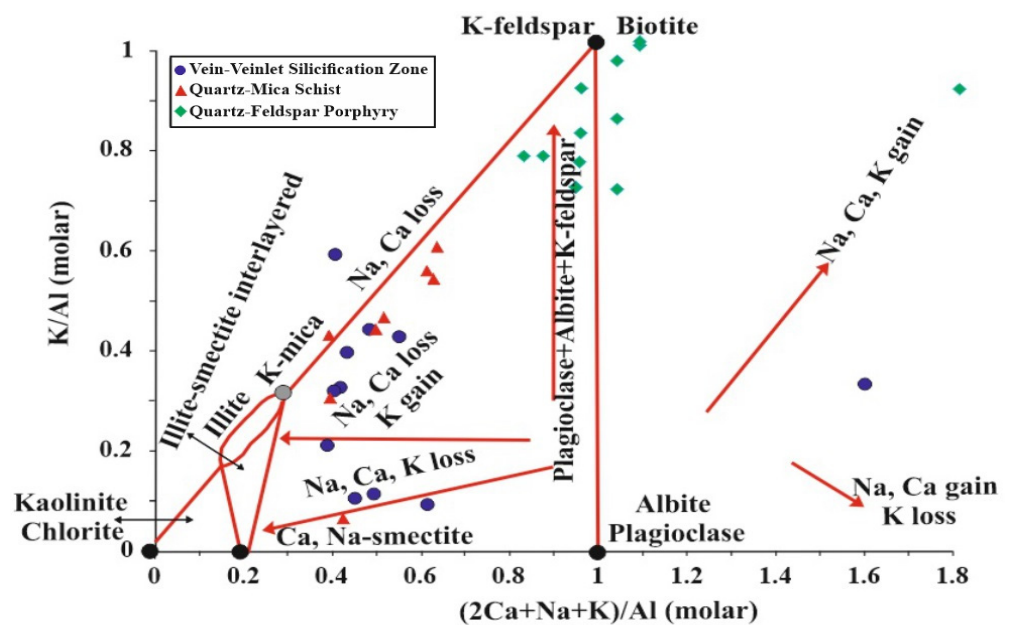


**Figure 15.** Vein–veinlet silicified zone, quartz–feldspar porphyry and quartz–mica schists  $(2Ca + Na + K)/Al$ – $K/Al$  molar element ratio graph, mass transfer and related alteration minerals [45].

The study area's alteration sample data are plotted using the molar  $K_2O/Al_2O_3$ – $Na_2O/Al_2O_3$  diagram of [41]. The vein–veinlet silicified zone is observed on the left side of the albite–muscovite line, on the right side of the quartz–feldspar porphyry line, and on both sides (left side strong-to-medium argillic alteration, right side strong-to-medium sericitic alteration). Additionally, quartz–mica schists are located on the albite–muscovite line (Figure 16a). The examined samples exhibit argillic, sericitic, and propylitic alteration, as evidenced by the presence of the chlorite, adularia, clay minerals, muscovite (sericite), and epidote mineral associations. Additionally, silicic alteration is observed in silica veins located near the  $Na_2O/Al_2O_3$   $y$ -axis. All samples analyzed fall below the plagioclase–K-feldspar (biotite) line, indicating depletion in  $Na_2O$  and enrichment in  $K_2O$ . The plot showing the molar ratio of  $K_2O/Al_2O_3$  versus  $MgO/Al_2O_3$  [41] demonstrates the relationship between muscovite and chlorite (Figure 16b). This suggests that muscovite (sericite) and minerals rich in K and Al (such as clay minerals, adularia, and alunite), and Al-enriched chlorite, are the most abundant minerals in altered rocks. As shown in Figure 16b, the vein–veinlet silicified zone is located in the low-Mg chloride field of the

plot, while the quartz–feldspar porphyry muscovite and the quartz–mica schist are mostly found in the field characterized by low-Mg chlorite and less muscovite.

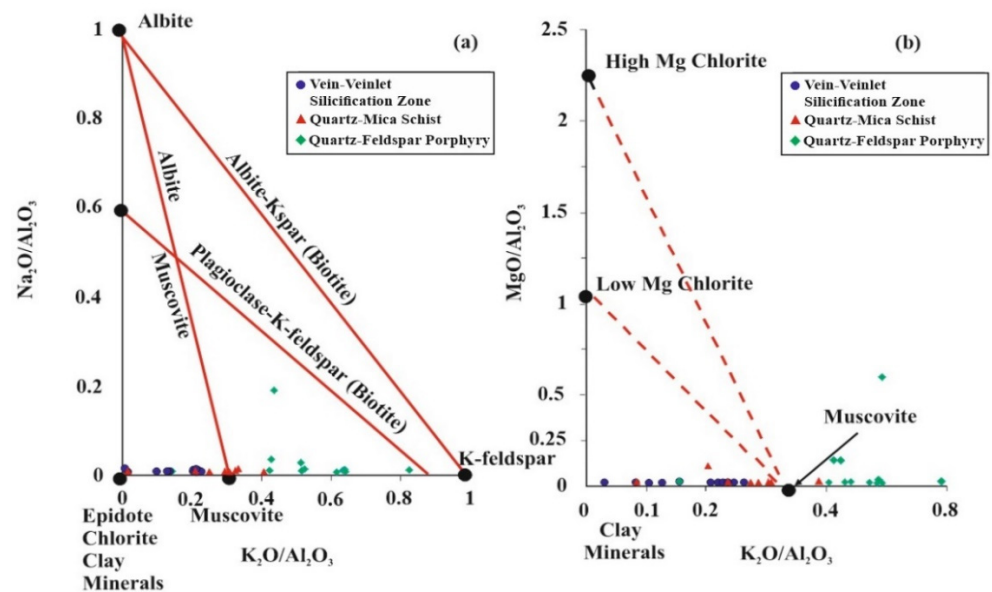


Figure 16. (a)  $\text{Na}_2\text{O}/\text{Al}_2\text{O}_3$ – $\text{K}_2\text{O}/\text{Al}_2\text{O}_3$ , (b)  $\text{MgO}/\text{Al}_2\text{O}_3$  vs.  $\text{K}_2\text{O}/\text{Al}_2\text{O}_3$  molar ratio plots [41].

The  $\text{TiO}_2$ – $\text{Al}_2\text{O}_3$  graph [35] indicates a single alteration trend from weak to strong for the silica vein, quartz–feldspar porphyry, and quartz–mica schist altered rocks (Figure 17).

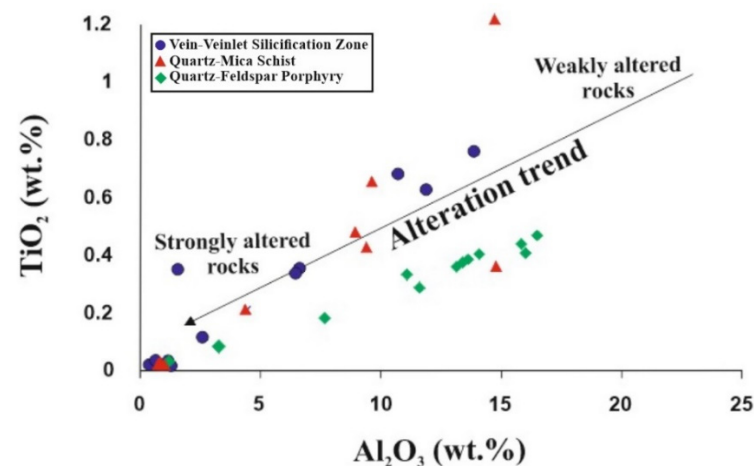
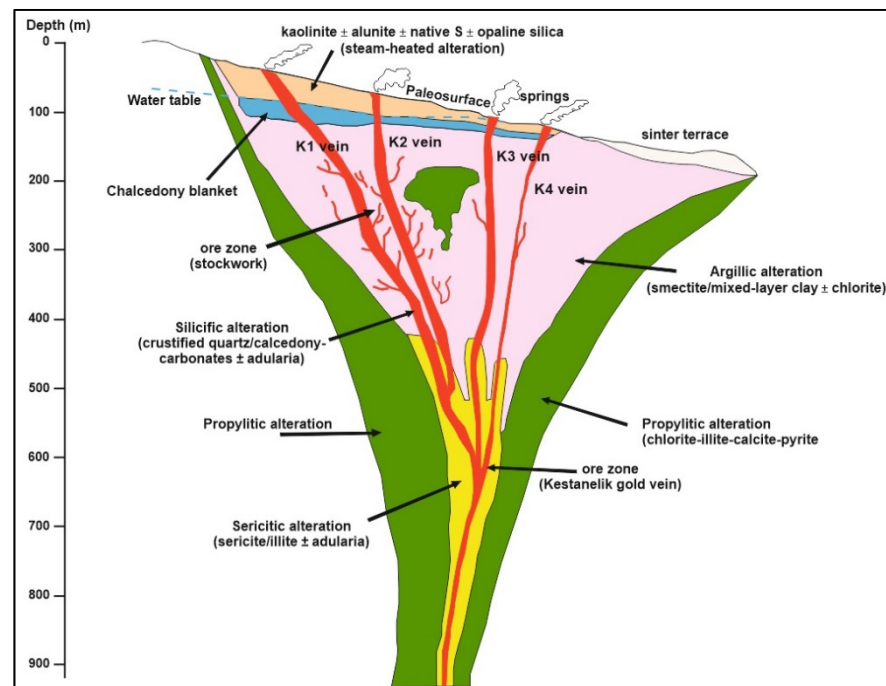


Figure 17.  $\text{TiO}_2$ – $\text{Al}_2\text{O}_3$  binary graph trends of weakly altered and strongly altered rocks [35].

## 6. Discussion

The Çamlıca metamorphic rocks, Kestanelik granodiorite, and Şahinli Formation volcanics in and around the Kestanelik Au mine deposit have undergone intense alteration. XRD results show the presence in all samples of mineral associations characterized by mainly quartz, illite/muscovite, and chlorite, with lesser amounts of calcite/dolomite, kaolinite, smectite, hematite, and alunite. These mineral assemblages and their various parageneses are similar to those observed in typical low-sulfidation epithermal deposits. Based on the petrographic studies, XRD results, and mass balance calculations, the gold-bearing silicified veins in the deposit display various types of hydrothermal alteration, including predominantly sericitic, argillic (K-metasomatic), and propylitic (Fe-rich chlorite), with lesser K-silicate, chloritization, and carbonation observed from the inside to the outside. Figure 18 shows a schematic model of the alteration zone halos of the Kestanelik

Au deposit, as presented in the genetic model developed by [13,91] for low-sulfidation epithermal gold deposits.



**Figure 18.** Schematic model showing the alteration zone halos of the Kestanelik low-sulfidation epithermal Au deposit.

These findings are based on field observations, mineral contents, mineral associations from polarizing microscope studies, and XRD analysis [22]. The alteration minerals and Au–silica in the alteration zone are assumed to have formed from hydrothermal processes that led to alteration of the metamorphic and granodiorite rocks. These processes were controlled by faults and fractures under specific temperature and acidic pH conditions. The presence of argillic (illite/muscovite) and advanced argillic (alunite + dickite/nacrite + pyrophyllite) alteration has been reported [3] in the vicinity of the study area. According to petrographic observations, silicification occurs in and around the main proximal alteration veins at Karatepe [92], located north of the study area. Additionally, quartz–sericite/illite ± adularia alteration surrounds the silicification zone. Furthermore, a distal to proximal change has been described in the silica ± smectite ± kaolinite ± Fe–Mg chlorite assemblage away from the mineralized veins. The outermost part of the alteration halo contains relatively less smectite and more Fe–Mg chlorite. In the argillic alteration zone of the Ovacık–Bergama Au–Ag deposit [28], biotite was transformed into Fe–Mg chlorite and smectite between 300 and 250 °C, pure illite was formed at 200 °C and pH 5–6, and silica was transported out to open the path for the hydrothermal system and to form the siliceous cap in and around the deposit. Smectite–illite mixed layers formed under acidic conditions (200–80 °C), and this allowed for the Au–silica mineralization. As the temperature decreased to 130 °C and the pH decreased to 3, the mineralized parts of the epithermal system and the non-ore rocks were affected. The precipitation of a silica cap in the Karaçayır kaolin deposit was caused by the release of silica during silicification processes, indicating hydrothermal activity within the rhyolitic tuffs and schists [31]. The silicified zones and Fe–oxyhydroxides were formed by alteration processes that occurred within kaolinized Miocene volcanics and Paleozoic shales.

The origin, temperature conditions, and hydrothermal activity of mineralization fluids have been determined for the Koru, Tesbihdere, and Kumarlar mineralization areas near the Kestanelik gold field [32]. The Kübler index for illites indicates low temperature (high-grade diagenesis) for the Koru deposit and high temperature for the Tesbihdere and Kumarlar deposits, and the major-trace element composition and low octahedral Mg + Fe contents are compatible with hydrothermal illites. The Çöpler Cu–Au deposit exhibits potassic, phyllic, propylitic, and, argillic (quartz + smectite + kaolinite), and advanced argillic (quartz + illite–smectite, quartz + crandallite + jarosite, and cristobalite) hydrothermal alteration zones in the Middle Eocene granodiorite–diorite porphyries and Late Paleozoic–Mesozoic metapelite–metacarbonate rocks [33].

Rare earth elements (REEs) play an important role in interpreting the nature of hydrothermal solutions that alter host rocks in and around mineralization. Although previously considered immobile, recent studies have shown that REEs can be mobilized through the circulation of hydrothermal fluid [93–95]. The distribution patterns of REEs in various rocks, as well as the abundance of light rare earth elements (LREEs) compared to heavy rare earth elements (HREEs), and the concentrations of REEs in all rocks, tend to decrease with increasing hydrothermal alteration intensity. Apparently, the hydrothermal fluids responsible for alteration in the Kestanelik Au deposit and host rocks had low REE contents, which were mobilized. Negative Eu anomalies are caused by the kaolinization of feldspars and micas and the chloritization of biotite and feldspars. It has been reported [32] that illites from the Tesbihdere and Kumarlar deposits have low chondrite-normalized abundances and negative Eu anomalies similar to the samples from the Kestanelik field. The alteration (hydrothermal and supergene) of granitic rocks in SW England may have caused the mobility of REEs, particularly trivalent REEs extracted from the system during K-silicate alteration, Eu lost during sericitic alteration, and light REEs removed from hydrothermal systems throughout chloritization and argillic alteration. Analysis of the separated minerals has revealed significant negative Eu anomalies in the micas and a positive Eu anomaly in the K-feldspar [92]. REEs were mobilized and fractionated during the supracrustal alteration of the Torrongo granodiorite, and the primary and moderately altered rocks are especially enriched in heavy REEs, whereas the strongly altered components are particularly depleted in heavy REEs. Furthermore, the mobility of REEs is likely controlled by pH variations in soil and groundwater. As different chemical environments are encountered, fractionation may also occur due to mineralogical controls [96].

Hydrothermal alteration results in significant variations in the elemental content and mineralogical composition of the host rocks through which hydrothermal fluids have circulated. These metasomatic exchange reactions can be calculated using various methods, such as mass exchange computations, alteration indices, and molar element ratios. Some researchers have frequently used molar element ratios to identify the dominant alteration minerals, which form through the replacement of primary minerals, mainly in magmatic rocks [8,49,50,97]. In a low-sulfidation epithermal system in New Zealand, the authors of [97] used the molar ratios of rock-forming elements in feldspars and phyllosilicate alteration minerals to determine the abundance of alteration minerals.

Molar elemental ratios indicate the presence of unaltered rocks, K gain, and Na–Ca loss, as well as the existence of illite–smectite–kaolinite associations. The ratios suggest the existence of illite–smectite–kaolinite when K/Al is between 0.2 and 0.33, less than 0.2, and equals zero, respectively.

The quartz–feldspar porphyry samples in the Kestanelik gold field fall within the range of  $2Ca + Na + K/Al$  and  $K/Al$  values of the feldspar compositions and biotite mixtures. Furthermore, the vein–veinlet silicified zone and quartz–mica schist samples fall into the K-mica area. The presence of alteration samples in these areas indicates sericitic and argillic alteration types. Additionally, there is propylitic alterations in quartz–feldspar porphyry and silicic alteration in silica veins resulting from the gains in Na, Ca, and K. According to the authors of [8], illite–smectite, illite, K-mica, and K-feldspar–biotite areas are found in the NW Iran Tarom–Hashtjin precious and base metal epithermal deposits,

indicating propylitic and argillic alteration types. Additionally, there is propylitic alteration in quartz–feldspar porphyry and silicic alteration in silica veins resulting from the gains in Na, Ca, and K.

In the vein–veinlet silicified zone, quartz–feldspar porphyry, and quartz–mica schist samples obtained from the Kestanelik Au deposit, the Ishikawa alteration index and chlorite–carbonate–pyrite index diagram show that the most abundant alterations were chlorite–pyrite, sericite–chlorite–pyrite, chlorite–pyrite–sericite, and chlorite–carbonate, and these indices also revealed the presence of argillic, chlorite, and propylitic alterations. Comparison of Na<sub>2</sub>O, K<sub>2</sub>O, Al<sub>2</sub>O<sub>3</sub>, CaO, MgO, and FeO contents of hydrothermal alteration samples in the Kestanelik gold deposit with the Ishikawa alteration index revealed mainly chlorite–sericite, and sericite mineral associations, and less adularia–sericite. This association indicates sericitic (argillic), propylitic, and adularia alteration types, which is characteristic of low-sulfidation epithermal deposits. In a previous study, the pyrite, sericite, and chlorite–carbonate in the epithermal vein samples of the Siah Jangal–Sar Kahno gold deposit in SE Iran tended to be argillic, sericite–carbonate, and clay minerals in most of the samples [6].

The diagram showing the sericitization index plotted against K<sub>2</sub>O + Na<sub>2</sub>O and CaO content indicates that all samples were within the hydrothermal alteration area and that the variation in the sericitization index indicates weak carbonation. It was reported [49] that the samples from the Zigana volcanics generally indicate some degree of hydrothermal alteration, according to the K<sub>2</sub>O + Na<sub>2</sub>O sericitization index. Additionally, carbonation is the dominant alteration type in the Arzular epithermal gold mineralization area, based on K<sub>2</sub>O + Na<sub>2</sub>O and CaO diagrams plotted for andesite samples [50].

Based on the chemical alteration index, the Kestanelik gold field mostly displays vein–veinlet silicified zone samples in the illite and smectite areas, quartz–feldspar porphyry samples in the muscovite, biotite, and smectite areas, and quartz–mica schist samples in the illite, muscovite, biotite, and smectite areas. The Al<sub>2</sub>O<sub>3</sub>–(Na<sub>2</sub>O + K<sub>2</sub>O)–(Fe<sub>2</sub>O<sub>3</sub> + MgO)–K<sub>2</sub>O triple diagram indicates that the vein–veinlet silicified zone and quartz–micaschist samples plot in the K-silicate, propylitic, and sericitic fields, while the quartz–feldspar porphyry mainly plots in the propylitic and less within the K-silicate field. The quartz–feldspar porphyry samples from the Kestanelik gold deposit plot within the range of 2Ca + Na + K/Al and K/Al values of the feldspar compositions and biotite mixtures. Additionally, the vein–veinlet silicified zone and quartz–mica schist samples fall into the K-mica field. The presence of alteration samples in these fields indicates sericitic and argillic alteration types. Additionally, there are propylitic alterations in quartz–feldspar porphyry and silicic alterations in silicified veins because of gains in Na, Ca, and K.

The diagram displaying the molar K<sub>2</sub>O/Al<sub>2</sub>O<sub>3</sub>–Na<sub>2</sub>O/Al<sub>2</sub>O<sub>3</sub> ratio indicates moderate to strong argillic and sericitic, silicic, and propylitic alterations. The K<sub>2</sub>O/Al<sub>2</sub>O<sub>3</sub>–MgO/Al<sub>2</sub>O<sub>3</sub> molar ratio plot shows the recovery of K and Al after the relationship between muscovite and chlorite. The molar ratio graph for the porphyry unit in the Karatepe sector shows that most of the data indicate interlayered illite–smectite, illite, and K-mica with high Na and Ca loss. This suggests a correlation between the proximity to Au mineralization and the gain and loss of K [89]. The TiO<sub>2</sub>–Al<sub>2</sub>O<sub>3</sub> graph shows a single trend from weak to strong for all rock groups in terms of hydrothermal alteration. In a previous study using this method [8], the main types of alteration in the Tarom–Hashtjin epithermal deposits were identified as argillic, sericitic, and propylitic. Similarly, the authors of [9] detected a single alteration trend from dioritic rocks and weakly altered rocks to strongly altered flysch host rocks and epithermal veins in the Siah Jangal–Sar Kahno epithermal gold deposit. Additionally, the authors of [6] reported moderate composition and mass gain when this method was applied to samples from the epithermal gold deposit.

## 7. Conclusions

The Kestanelik gold deposit is a low-sulfidation epithermal deposit that developed during intense hydrothermal alteration. Alterations primarily occurred in metamorphic rocks and granodiorite and occurred less often in volcanic rocks. Mineralization was controlled by silicified veins, stockwork veinlets, and tectonic elements.

The dominant alteration type observed in the central area of the chlorite–pyrite zone is the silicified vein and breccia system that contains ore. The ore is frequently located in close proximity to fluid channels. Trending toward the periphery, the ore mineralization is surrounded by zones of sericite–chlorite–pyrite, chlorite–pyrite–sericite, and chlorite–carbonate alteration mineral assemblages.

The Kestanelik Au mineralization was accompanied by hydrothermal fluids that caused alteration, including REE mobilization, kaolinization of feldspars and micas, and chloritization of biotite and feldspars. This alteration likely resulted in negative Eu anomalies.

Results from the mass balance calculations indicate that analyzing intensely to moderately altered source rocks is a valuable method for measuring elemental changes during metasomatic reactions.

The petrographic studies and mass balance calculations based on the analysis of geochemical characteristics indicate the type and intensity of hydrothermal alteration. The zoned alteration comprises silicic, argillic (K-metasomatic), sericitic, and propylitic (Fe-rich chlorite) types, which are commonly found in epithermal ore systems.

The chemical composition of the hydrothermal fluid was investigated by calculating the elemental gains and losses. The results show that the fluid was enriched in Si, K, and Al, but depleted in Na and Ca.

The Ishikawa alteration index and chlorite–carbonate–pyrite index were effective in determining alteration types. Additionally, the sericitization index and chemical alteration index provided helpful information.

**Author Contributions:** Fieldwork, D.K. and O.C.; conceptualization, D.K. and O.C.; methodology, O.C.; investigation, D.K. and O.C.; writing—original draft preparation, review and editing, D.K. and O.C.; visualization and formal analysis, D.K. All authors have read and agreed to the published version of the manuscript.

**Funding:** This research was a part of D. Kıray’s doctoral study and was funded by the Süleyman Demirel University Scientific Research Project Office (BAP, project no: 3574–D2-13).

**Data Availability Statement:** Data are contained within the article.

**Acknowledgments:** The authors thank Tümad-Mining Inc. (Ankara, Turkey) and Chesser Resources Inc. (Brisbane, Australia) for helping with field studies and supplying drilling core samples. The authors would like to thank Ahmet Yıldız for his assistance in identifying the XRD graphics, and the reviewers for their valuable contributions to improving this paper.

**Conflicts of Interest:** The authors declare no conflicts of interest.

## Appendix A

**Table A1.** Major- and minor oxide, compositions with trace and rare earth element contents of the drilling samples from the study area [22].

Major Oxides (wt.%)	Silicified Vein											
	DL	KED 2-2	KED2-6	KED2-7	KED2-13	KED17-8	KED63-2	KED63-3	KED63-5	KED63-9	KED63-10	KED63-11
SiO <sub>2</sub>	0.01	96.32	84.32	96.50	98.02	95.37	74.04	57.74	83.90	93.53	86.04	69.14
Al <sub>2</sub> O <sub>3</sub>	0.01	1.20	6.67	1.23	0.55	0.97	11.89	10.85	6.41	1.19	6.36	14.33
Fe <sub>2</sub> O <sub>3</sub>	0.04	0.77	3.18	0.60	0.61	1.45	4.49	8.03	3.87	3.46	3.09	6.09
MgO	0.01	0.09	0.76	0.05	0.04	0.04	1.90	4.13	1.07	0.10	0.41	1.79
CaO	0.01	0.06	0.06	0.06	0.10	0.10	0.29	4.75	0.13	0.13	0.09	0.12
Na <sub>2</sub> O	0.01	0.02	0.07	0.02	<0.01	0.01	0.42	0.16	0.06	0.02	0.06	0.24
K <sub>2</sub> O	0.01	0.20	1.84	0.17	0.03	0.09	3.11	2.54	1.51	0.13	1.35	3.59
TiO <sub>2</sub>	0.01	0.05	0.37	0.02	<0.01	<0.01	0.57	0.64	0.36	0.02	0.31	0.75
P <sub>2</sub> O <sub>5</sub>	0.01	0.02	0.05	<0.01	<0.01	0.02	0.13	0.16	0.07	0.02	0.03	0.10
MnO	0.01	0.01	0.02	<0.01	<0.01	<0.01	0.11	0.47	0.03	0.02	<0.01	0.03
Cr <sub>2</sub> O <sub>3</sub>	0.002	0.002	0.022	0.002	<0.002	<0.002	0.015	0.013	0.012	<0.002	0.009	0.015
Total/C	0.02	0.02	0.04	0.02	0.03	0.03	0.03	2.54	0.04	0.07	0.04	0.10
Total/S	0.02	<0.02	<0.02	<0.02	<0.02	0.46	0.07	0.13	<0.02	<0.02	<0.02	<0.02
LOI	0.1	1.20	2.60	1.30	0.60	1.47	2.90	10.30	2.50	1.35	2.20	3.6
Total	0.01	99.94	99.96	99.95	99.95	99.98	99.94	99.91	99.92	99.97	99.95	99.80
<b>Trace-REE (ppm)</b>												
Ba	1	199.00	225.00	18.000	252.00	27.00	428.00	305.00	173.00	21.00	165.00	405.00
Rb	0.1	0.20	2.50	0.20	<0.10	0.20	2.90	3.20	2.00	0.10	1.80	4.5
Sr	0.5	1.80	6.60	0.90	0.50	0.60	9.40	10.00	6.10	0.60	5.50	13.3
Nb	0.1	12.70	90.90	11.90	4.00	7.20	99.90	106.90	72.90	11.50	71.90	173.6
Hf	0.1	12.60	27.00	17.30	10.00	20.30	14.90	44.40	21.20	14.10	23.70	59.2
Ta	0.1	0.60	4.40	0.70	<0.20	<0.20	6.50	9.60	5.60	0.90	4.60	9.8

Table A1. Cont.

Silicified Vein												
Trace-REE (ppm)												
V	8	12.00	61.00	<8.00	<8.00	20.00	107.00	119.00	60.00	19.00	63.00	125
Zr	0.1	7.60	89.70	6.30	2.00	5.10	104.50	115.70	78.70	4.50	69.50	165.0
Y	0.1	1.70	23.00	5.90	0.20	10.40	14.50	24.90	19.10	1.80	14.70	25.4
Cu	0.1	15.80	11.30	9.70	6.80	20.10	62.30	75.90	16.20	8.30	9.50	18.1
Pb	0.1	171.30	57.9	93.50	65.30	60.90	18.40	44.50	16.60	28.90	20.00	17.9
Zn	1	65.00	86.000	32.00	18.00	25.00	62.00	88.00	54.00	24.00	21.00	86
As	0.5	15.20	36.40	10.10	9.70	615.20	37.00	37.60	48.60	318.10	151.10	41.8
Sb	0.1	5.80	12.00	4.70	1.50	17.20	21.20	3.10	25.00	258.00	76.30	15.7
Ag	0.1	2.40	0.20	0.70	1.00	2.90	<0.10	0.30	0.20	0.50	0.50	0.3
Au (ppb)	0.5	266.20	80.80	64.70	434.20	7060.70	4.00	2.50	140.10	95.20	432.00	42.8
Hg	0.01	0.08	0.02	0.05	0.02	0.09	0.11	0.05	0.02	0.06	0.05	0.04
La	0.1	2.10	16.20	2.20	0.60	2.20	14.20	25.90	18.00	2.50	17.80	27.7
Ce	0.1	2.50	32.70	3.50	0.50	3.00	29.80	48.50	32.80	3.00	33.20	56.6
Pr	0.02	0.32	3.77	0.47	0.08	0.39	3.36	5.84	3.79	0.38	3.84	6.33
Nd	0.30	1.40	14.30	1.80	0.30	1.70	12.10	22.50	14.20	1.40	14.70	22.6
Sm	0.05	0.35	3.04	0.49	0.16	0.60	2.85	4.66	3.06	0.41	3.01	4.53
Eu	0.02	0.07	0.64	0.16	0.02	0.29	0.73	1.16	0.79	0.11	0.78	1.09
Gd	0.05	0.58	3.13	0.92	0.36	1.31	2.84	5.01	3.22	0.57	2.95	4.44
Tb	0.01	0.04	0.54	0.12	0.02	0.21	0.44	0.81	0.52	0.07	0.44	0.74
Dy	0.05	0.28	3.36	0.72	0.10	1.43	2.45	4.43	3.15	0.37	2.54	4.37
Ho	0.02	0.06	0.75	0.19	<0.02	0.30	0.56	0.90	0.68	0.07	0.47	0.90
Er	0.03	0.21	2.13	0.52	0.03	0.88	1.77	2.76	1.97	0.20	1.47	2.58
Tm	0.01	0.03	0.33	0.08	0.01	0.12	0.25	0.41	0.28	0.04	0.21	0.39
Yb	0.05	0.17	1.98	0.54	0.10	0.81	1.87	2.74	1.80	0.19	1.49	2.71
Lu	0.01	0.04	0.28	0.09	0.02	0.12	0.30	0.40	0.27	0.03	0.24	0.40

Table A1. Cont.

Quartz–Feldspar–Porphyry													
Major Oxides (wt.%)	DL	KED6-3	KED6-4	KED6-5	KED6-6	KED6-7	KED6-8	KED6-10	KED17-1	KED17-2-	KED17-6	KED17-7	KED135-3
SiO <sub>2</sub>	0.01	67.88	70.41	69.97	67.10	71.32	6618	73.71	64.79	75.49	89.52	83.08	67.69
Al <sub>2</sub> O <sub>3</sub>	0.01	14.99	13.77	13.45	16.39	13.62	14.04	11.48	16.00	11.92	3.34	7.37	16.61
Fe <sub>2</sub> O <sub>3</sub>	0.04	3.05	3.61	2.52	2.59	2.79	3.48	3.46	4.57	2.10	3.35	2.35	2.31
MgO	0.01	1.51	1.30	0.89	0.94	0.90	1.15	0.83	1.03	0.38	0.10	0.47	0.56
CaO	0.01	0.30	0.33	0.26	0.31	0.34	0.28	0.22	0.35	0.13	0.07	0.15	0.17
Na <sub>2</sub> O	0.01	2.82	1.30	0.31	0.71	1.16	0.34	0.69	0.25	0.19	0.09	0.08	0.25
K <sub>2</sub> O	0.01	7.00	6.61	8.90	8.27	6.68	9.21	6.79	9.03	6.89	2.06	4.34	8.13
TiO <sub>2</sub>	0.01	0.36	0.40	0.39	0.44	0.40	0.42	0.35	0.45	0.34	0.08	0.19	0.48
P <sub>2</sub> O <sub>5</sub>	0.01	0.14	0.14	0.13	0.15	0.13	0.14	0.12	0.13	0.03	0.03	0.05	0.05
MnO	0.01	0.07	0.07	0.05	0.04	0.05	0.06	0.05	0.03	0.01	<0.01	0.03	0.02
Cr <sub>2</sub> O <sub>3</sub>	0.002	0.004	<0.002	<0.002	<0.002	<0.002	<0.002	<0.002	<0.002	<0.002	<0.002	<0.002	<0.002
Total/C	0.02	0.02	0.03	0.02	0.03	0.03	0.06	<0.02	0.04	0.04	0.04	0.03	<0.02
Total/S	0.02	0.45	0.05	0.62	0.38	0.11	1.22	1.22	<0.02	<0.02	0.54	<0.02	<0.02
LOI	0.1	1.31	1.90	2.35	2.51	2.50	3.30	0.95	3.20	2.40	0.78	1.80	3.60
Total	0.01	99.88	99.89	99.84	99.83	99.97	99.82	99.87	99.83	99.88	99.96	99.91	99.87
<b>Trace-REE (ppm)</b>													
Ba	1	230.00	670.00	674.00	791.00	668.00	647.00	583.00	836.00	575.00	190.00	142.00	866.00
Rb	0.1	3.50	3.30	3.10	3.30	3.00	3.00	2.60	3.20	2.80	0.60	1.40	2.90
Sr	0.5	3.70	6.40	6.30	7.10	6.70	6.30	5.50	7.10	5.70	2.00	3.00	6.70
Nb	0.1	365.00	315.80	426.70	404.40	319.70	442.20	307.50	420.60	325.50	97.20	217.00	371.80
Hf	0.1	65.60	159.00	124.70	114.30	171.80	143.40	72.20	78.60	90.30	30.80	36.90	96.60
Ta	0.1	3.90	9.10	10.00	11.10	9.70	9.60	9.10	10.80	8.10	2.40	4.30	10.80
V	8	50.00	76.00	74.00	74.00	68.00	74.00	59.00	83.00	51.00	23.00	43.00	75.00

Table A1. Cont.

Quartz–Feldspar–Porphyry													
Trace-REE (ppm)													
Zr	0.1	134.90	121.30	105.60	113.20	108.30	109.50	99.00	113.60	93.00	19.60	53.40	109.00
Y	0.1	26.00	10.50	11.60	13.90	14.50	13.60	12.00	12.30	10.30	4.10	8.60	12.20
Cu	0.1	12.80	10.40	12.40	16.10	26.60	34.60	9.30	8.30	7.10	22.50	20.80	6.60
Pb	0.1	60.90	35.90	53.40	29.40	13.50	102.10	32.40	31.40	34.70	69.60	46.80	7.20
Zn	1	93.00	49.00	34.00	31.00	32.00	54.00	40.00	97.00	33.00	26.00	62.00	22.00
As	0.5	413.70	5.50	340.90	458.20	175.50	1376.50	213.60	154.20	85.60	356.00	68.40	43.60
Sb	0.1	7.30	1.00	10.60	8.20	3.90	28.80	3.00	23.00	9.80	19.40	14.70	6.60
Ag	0.1	0.20	0.10	0.20	0.40	0.20	0.30	0.70	0.20	0.20	2.60	0.30	0.10
Au (ppb)	0.5	26.10	39.60	25.70	2.30	2.40	59.20	436.00	71.10	171.50	1205.10	461.20	136.20
Hg	0.01	0.11	0.03	0.29	0.24	0.11	0.66	0.10	0.01	0.02	0.16	0.03	<0.01
La	0.1	13.50	20.60	22.30	26.00	20.50	25.00	22.30	21.20	20.70	7.50	11.20	23.60
Ce	0.1	26.30	37.10	39.70	47.80	37.10	45.30	39.10	38.90	34.10	12.60	20.00	40.20
Pr	0.02	3.40	4.02	4.28	5.08	3.85	5.06	4.32	4.57	3.78	1.43	2.18	4.49
Nd	0.30	11.20	14.80	14.70	18.30	13.10	18.20	16.00	16.50	13.40	5.70	8.00	16.30
Sm	0.05	2.58	2.95	2.93	3.42	2.87	3.65	2.95	3.13	2.70	1.09	1.60	3.44
Eu	0.02	0.75	0.80	0.80	1.09	0.79	0.96	0.82	0.92	0.77	0.22	0.44	0.85
Gd	0.05	2.97	2.84	2.68	3.40	2.74	3.30	2.93	2.98	2.59	1.12	1.75	2.98
Tb	0.01	0.55	0.39	0.40	0.47	0.42	0.47	0.40	0.42	0.37	0.13	0.25	0.41
Dy	0.05	3.55	1.99	2.01	2.52	2.39	2.53	2.19	2.43	1.98	0.78	1.33	2.18
Ho	0.02	0.82	0.37	0.43	0.49	0.55	0.49	0.43	0.52	0.38	0.13	0.31	0.45
Er	0.03	2.32	1.12	1.17	1.49	1.56	1.43	1.24	1.43	1.19	0.43	0.89	1.24
Tm	0.01	0.37	0.19	0.20	0.27	0.25	0.22	0.19	0.23	0.18	0.06	0.15	0.18
Yb	0.05	2.30	1.30	1.28	1.59	1.59	1.56	1.40	1.63	1.21	0.44	0.95	1.48
Lu	0.01	0.37	0.21	0.20	0.28	0.24	0.25	0.23	0.27	0.19	0.09	0.15	0.23

Table A1. Cont.

Quartz–Mica Schist									
Major Oxides (wt.%)	DL	KED2-5	KED2-11	KED6-11	KED44-2	KED44-3	KED44-12	KED70-1	KED70-2
SiO <sub>2</sub>	0.01	90.65	95.19	80.37	87.95	78.10	52.92	95.78	71.54
Al <sub>2</sub> O <sub>3</sub>	0.01	2.79	1.88	9.22	4.66	8.78	14.85	1.19	9.37
Fe <sub>2</sub> O <sub>3</sub>	0.04	2.88	1.15	2.91	2.67	4.66	14.06	0.65	7.92
MgO	0.01	0.21	0.16	0.49	0.73	2.00	4.78	0.09	3.08
CaO	0.01	0.004	0.06	0.09	0.13	0.15	0.44	0.07	0.17
Na <sub>2</sub> O	0.01	0.03	0.03	0.09	0.03	0.04	0.06	0.01	0.03
K <sub>2</sub> O	0.01	0.99	0.37	3.61	1.60	2.44	3.56	0.11	2.77
TiO <sub>2</sub>	0.01	0.13	0.07	0.45	0.22	0.50	1.63	0.01	0.68
P <sub>2</sub> O <sub>5</sub>	0.01	0.07	0.02	0.06	0.05	0.07	0.15	0.07	0.09
MnO	0.01	0.02	0.02	<0.01	0.01	0.03	0.07	<0.01	0.04
Cr <sub>2</sub> O <sub>3</sub>	0.002	0.008	0.004	0.010	0.004	0.035	0.036	<0.002	0.030
Total/C	0.02	0.08	0.03	0.04	<0.02	0.03	0.02	0.79	0.07
Total/S	0.02	0.06	<0.02	<0.02	<0.02	<0.02	<0.02	<0.02	<0.02
LOI	0.1	2.10	1.00	2.60	1.90	3.10	7.20	2.00	4.10
Total	0.01	99.98	99.95	99.90	99.95	99.91	99.77	99.98	99.82
<b>Trace-REE (ppm)</b>									
Ba	1	90.00	92.00	281.00	120.00	279.00	95.00	36.00	208.00
Rb	0.1	0.80	0.60	3.30	1.30	2.80	2.80	0.20	2.30
Sr	0.5	2.50	1.70	8.60	4.10	8.90	1.80	0.40	11.00
Nb	0.1	49.40	21.80	191.10	67.80	113.00	177.80	10.20	132.40
Hf	0.1	16.20	19.00	58.00	24.50	18.40	75.20	149.60	47.60
Ta	0.1	2.10	1.00	6.70	4.00	6.60	<0.20	0.80	5.90
V	8	25.00	18.00	71.00	41.00	75.00	319.00	10.00	103.00

Table A1. Cont.

Quartz–Mica Schist										
Trace-REE (ppm)										
Zr	0.1	33.90	24.10	129.70	47.30	105.00	100.50	6.0	94.60	
Y	0.1	5.30	2.70	14.60	13.10	20.50	30.10	4.000	17.50	
Cu	0.1	33.50	15.90	13.90	16.70	22.30	40.60	54.60	33.70	
Pb	0.1	128.10	95.10	27.90	24.80	13.70	21.80	26.00	28.00	
Zn	1	49.00	54.00	21.00	38.00	88.00	128.00	16.00	101.00	
As	0.5	169.80	16.10	99.50	105.60	118.60	326.20	10.90	422.40	
Sb	0.1	7.80	3.60	18.90	25.80	17.00	40.70	8.90	58.90	
Ag	0.1	0.70	0.70	0.30	0.20	<0.10	0.20	10.40	0.40	
Au (ppb)	0.5	376.40	376.70	552.1	79.4	18.70	128.00	903.10	158.10	
Hg	0.01	0.06	0.04	0.04	0.01	<0.01	0.020	2.87	0.02	
La	0.1	7.60	2.40	19.5	19.6	23.30	3.70	5.20	22.90	
Ce	0.1	11.30	3.40	37.6	33.8	45.40	6.50	6.70	43.80	
Pr	0.02	1.19	0.54	4.51	4.58	5.54	1.23	0.84	5.02	
Nd	0.30	4.40	2.00	17.5	17.0	21.80	6.30	4.00	19.90	
Sm	0.05	0.99	0.55	3.57	3.37	4.29	2.19	1.10	4.03	
Eu	0.02	0.20	0.10	0.75	0.74	0.94	0.74	0.24	0.85	
Gd	0.05	1.04	0.72	3.13	3.08	4.19	3.87	1.12	3.85	
Tb	0.01	0.15	0.08	0.47	0.41	0.62	0.76	0.12	0.57	
Dy	0.05	0.88	0.48	2.47	2.21	3.30	5.10	0.64	3.07	
Ho	0.02	0.20	0.09	0.56	0.44	0.69	1.17	0.13	0.64	
Er	0.03	0.58	0.25	1.58	1.28	2.01	3.31	0.35	1.84	
Tm	0.01	0.10	0.05	0.24	0.20	0.30	0.50	0.05	0.27	
Yb	0.05	0.67	0.29	1.74	1.30	1.92	3.27	0.31	1.77	
Lu	0.01	0.11	0.05	0.25	0.21	0.32	0.50	0.05	0.27	

## References

1. Berger, B.R.; Bonham, H.F., Jr. Epithermal gold-silver deposits in the western United States: Time-space products of evolving plutonic, volcanic and tectonic environments. *J. Geochem. Explor.* **1990**, *36*, 103–142. [[CrossRef](#)]
2. Yılmaz, H.; Oyman, T.; Arehart, G.A.; Çolakoğlu, R.; Billor, Z. Low-sulfidation type Au–Ag mineralization at Bergama, Izmir, Turkey. *Ore Geol. Rev.* **2007**, *32*, 81–124. [[CrossRef](#)]
3. Yılmaz, H.; Oyman, T.; Sönmez, F.N.; Arehart, G.B.; Billor, Z. Intermediate sulfidation epithermal gold-base metal deposits in Tertiary subaerial volcanic rocks Şahinli/Tespil Dere (Lapseki/Western Turkey). *Ore Geol. Rev.* **2010**, *37*, 236–258. [[CrossRef](#)]
4. Ünal İmer, E.; Güleç, N.; Kuşcu, İ.; Fallick, A.E. Genetic investigation and comparison of Kartaladag and Madendag epithermal gold deposits in Çanakkale, NW Turkey. *Ore Geol. Rev.* **2013**, *53*, 204–222. [[CrossRef](#)]
5. Liu, Z.; Mao, X.; Deng, H.; Li, B.; Zhang, S.; Lai, J.; Bayless, R.C.; Pan, M.; Li, L.; Shang, Q. Hydrothermal processes at the Axi epithermal Au deposit, Western Tianshan: Insights from geochemical effects of alteration, mineralization and trace elements in pyrite. *Ore Geol. Rev.* **2018**, *102*, 368–385. [[CrossRef](#)]
6. Najaran, M.; Mehrabi, B.; Siani, M.G. Mineralogy, hydrothermal alteration, fluid inclusion, and O–H stable isotopes of the Siah Jangal-Sar Kahno epithermal gold deposit, SE Iran. *Ore Geol. Rev.* **2020**, *125*, 103689. [[CrossRef](#)]
7. Novruzov, N.; Valiyev, A.; Bayramov, A.; Mammadov, S.; Ibrahimov, J.; Ebdulrehimli, A. Mineral composition and paragenesis of altered and mineralized zones in the Gadir low sulfidation epithermal deposit (Lesser Caucasus, Azerbaijan). *Iran. J. Earth Sci.* **2019**, *11*, 14–29.
8. Siani, M.G.; Lentz, D.R. Litho-geochemistry of various hydrothermal alteration types associated with precious and base metal epithermal deposits in the Tarom-Hashtjin metallogenic province, NW Iran: Implications for regional exploration. *J. Geochem. Explor.* **2022**, *232*, 106903. [[CrossRef](#)]
9. Simpson, M.P.; Gazley, M.F.; Stuart, A.G.; Pearce, M.A.; Birchall, R.; Chappell, D.; Christie, A.B.; Stevens, M.R. Hydrothermal alteration at the Karangahake epithermal Au–Ag deposit, Hauraki Goldfield, New Zealand. *Econ. Geol.* **2019**, *114*, 243–273. [[CrossRef](#)]
10. Taylor, B.E. Epithermal gold deposits. In *Mineral Deposits of Canada: A Synthesis of Major Deposits-Types, District Metallogeny, the Evolution of Geological Provinces, and Exploration Methods*; Goodfellow, W.D., Ed.; Special Publication N. 5; Geological Association of Canada, Mineral Deposits Division: St. John's, NL, Canada, 2007; pp. 113–139.
11. White, N.C.; Hedenquist, J.W. Epithermal gold deposits: Styles, characteristics and exploration. *SEG News.* **1995**, *23*, 9–13. [[CrossRef](#)]
12. Evans, A.M. *Ore Geology and Industrial Minerals: An Introduction*; Blackwell Publ.: Oxford, UK, 1993; p. 389.
13. Hedenquist, J.W.; Arribas, R.A.; Gonzalez-Urien, E. Exploration for epithermal gold deposits. *Soc. Econ. Geol. Rev.* **2000**, *13*, 245–277.
14. Duba, D.; Williams-Jones, A.E. The application of illite crystallinity, organic-matter reflectance, and isotopic techniques to mineral exploration—A case-study in southwestern Gaspé, Quebec. *Econ. Geol.* **1983**, *78*, 1350–1363. [[CrossRef](#)]
15. Kelley, D.L.; Kelley, K.D.; Coker, W.B.; Caughlin, B.; Doherty, M.E. Beyond the obvious limits of ore deposits: The use of mineralogical, geochemical, and biological features for the remote detection of mineralization. *Econ. Geol.* **2006**, *101*, 729–752. [[CrossRef](#)]
16. Meyer, C.; Hemley, J.J. *Wall Rock Alteration in Geochemistry of Ore Deposits*; Barnes, H.L., Ed.; Holt, Rinehart and Winston: New York, NY, USA, 1967; pp. 166–235.
17. Yoneda, T.; Mokko, H.; Matsumoto, A.; Sato, T. Comparison of smectite–corrensite–chlorite series minerals in the Todoroki and Hishikari Au–Ag deposits: Applicability of mineralogical properties as exploration index for epithermal systems. *Nat. Resour. Res.* **2021**, *30*, 2889–2908. [[CrossRef](#)]
18. Guo, N.; Guo, W.; Shi, W.; Huang, Y.; Guo, Y.; Lian, D. Characterization of illite clays associated with the Sinongduo low sulfidation epithermal deposit, Central Tibet using field SWIR spectrometry. *Ore Geol. Rev.* **2020**, *120*, 103228. [[CrossRef](#)]
19. Rose, A.W.; Burt, D.M. Hydrothermal alteration. In *Geochemistry of Hydrothermal Ore Deposits*; Barnes, H.L., Ed.; John Wiley & Sons: New York, NY, USA, 1979; pp. 173–235.
20. Chen, M.T.; Wei, J.H.; Li, Y.J.; Shi, W.J.; Liu, N.Z. Epithermal gold mineralization in Cretaceous volcanic belt, SE China: Insight from the Shangshangang deposit. *Ore Geol. Rev.* **2020**, *118*, 103355. [[CrossRef](#)]
21. Prihatmoko, S.; Idrus, A. Low sulfidation epithermal gold deposits in Java, Indonesia: Characteristic and linkage to the volcano-tectonic setting. *Ore Geol. Rev.* **2020**, *121*, 103490. [[CrossRef](#)]
22. Kiray, D. Determination of the Origin of Kestanelik Au–Ag Mineralization in Şahinli (Lapseki–Çanakkale, Western Turkey) Region by Geological, Mineralogical and Geochemical Investigations. Ph.D. Thesis, Süleyman Demirel University, Isparta, Turkey, 2021; p. 217.
23. Bakhsh, R.A.; Ahmed, A.H. The Umm Matierah gold prospect: Mineralogical and geochemical characteristics of a potential low-sulfidation epithermal gold deposits, southeastern Arabian Shield, Saudi Arabia. *J. Asian Earth Sci.* **2023**, *9*, 100153. [[CrossRef](#)]
24. Mikaeili, K.; Hosseinzadeh, M.R.; Moayyed, M.; Maghfouri, S. The Shah-Ali-Beiglou Zn–Pb–Cu (–Ag) deposit, Iran: An example of intermediate sulfidation epithermal type mineralization. *Minerals* **2018**, *8*, 148. [[CrossRef](#)]
25. İmer, A.; Richards, J.P.; Muehlenbachs, K. Hydrothermal evolution of the Çöpler porphyry-epithermal Au deposit, Erzincan Province, central eastern Turkey. *Econ. Geol.* **2016**, *111*, 1619–1658. [[CrossRef](#)]

26. Kiray, D.; Cengiz, O. Petrographical and geochemical characteristics of the Kestanelik granitoid (Çanak kale, Biga Peninsula). *Geol. Bull. Turk.* **2023**, *66*, 127–148.
27. Gürler, Z. Karadere Low Sulfidation Gold Deposit (İvrindi, Balıkesir): An example for Detachment Fault-Related Epithermal Gold Deposits in Western Turkey. Master's Thesis, Balıkesir University, Balıkesir, Turkey, 2019; p. 100.
28. Dill, H.G.; Dohrmann, R.; Kaufhold, S.; Çiçek, G. Mineralogical, chemical and micromorphological studies of the argillic alteration zone of the epithermal gold deposit Ovacik, Western Turkey: Tools for applied and genetic economic geology. *J. Geochem. Explor.* **2015**, *148*, 105–127. [[CrossRef](#)]
29. Carrillo-Rosúa, J.; Morales-Ruano, S.; Esteban-Arispe, I.; Hach-Ali, P.F. Significance of phyllosilicate mineralogy and mineral chemistry in an epithermal environment. Insights from the Palai-Islica Au-Cu deposit (Almeria, SE Spain). *Clays Clay Miner.* **2009**, *57*, 1–24. [[CrossRef](#)]
30. Cravero, F.; Dominguez, E.; Iglesias, C. Genesis and applications of the Cerro Rubio kaolin deposit, Patagonia Argentina. *Appl. Clay Sci.* **2001**, *18*, 157–172. [[CrossRef](#)]
31. Kadir, S.; Erkoyun, H. Genesis of the hydrothermal Karaçayır kaolinite deposit in Miocene volcanics and Palaeozoic metamorphic rocks of the Uşak-Güre Basin, western Turkey. *Turk. J. Earth Sci.* **2013**, *22*, 444–468. [[CrossRef](#)]
32. Bozkaya, Ö.; Bozkaya, G.; Uysal, İ.T.; Banks, D.A. Illite occurrences related to volcanic-hosted hydrothermal mineralization in the Biga Peninsula, NW Turkey: Implications for the age and origin of fluids. *Ore Geol. Rev.* **2016**, *76*, 35–51. [[CrossRef](#)]
33. Bozkaya, Ö.; Bozkaya, G.; Haniçlı, N.; Güven, A.S.; Banks, D.A.; Uysal, İ.T. Mineralogical evidences on argillic alteration in the Çöpler porphyry-epithermal gold deposit (Erzincan, East-Central Anatolia). *Geol. Bull. Turk.* **2018**, *31*, 335–358.
34. Schalamuck, I.B.; Zubia, M.; Genini, A.; Fernandez, R.R. Jurassic epithermal Au-Ag deposits of Patagonia, Argentina. *Ore Geol. Rev.* **1997**, *305*, 57–71. [[CrossRef](#)]
35. Gresens, R.L. Composition volume relationships of metasomatism. *Chem. Geol.* **1967**, *2*, 47–65. [[CrossRef](#)]
36. Ishikawa, Y.; Sawaguchi, T.; Iwaya, S.; Horiuchi, M. Delineation of prospecting targets for Kuroko deposits based on models of volcanism of underlying dacite and alteration haloes. *Min. Geol.* **1976**, *26*, 105–117.
37. Nesbitt, H.W.; Young, G.M. Early Proterozoic climates and plate motions inferred from major element chemistry of lutites. *Nature* **1982**, *299*, 715–717. [[CrossRef](#)]
38. Myers, R.E.; MacLean, W.H. The geology of the New Inco copper deposit, Noranda District, Quebec. *Can. J. Earth Sci.* **1983**, *20*, 1291–1304. [[CrossRef](#)]
39. MacLean, W.H.; Hoy, L.D. Geochemistry of hydrothermally altered rocks at the Horne mine, Noranda, Quebec. *Econ. Geol.* **1991**, *86*, 506–528. [[CrossRef](#)]
40. Davies, J.F.; Whitehead, R.E. Molar ratios in the study of unaltered and hydrothermally altered greywackes and shales. *Chem. Geol.* **1994**, *111*, 85–100. [[CrossRef](#)]
41. Davies, J.F.; Whitehead, R.E. Alkali-alumina and MgO-alumina molar ratios of altered and unaltered rhyolites. *Explor. Min. Geol.* **2006**, *15*, 75–88. [[CrossRef](#)]
42. Davies, J.F.; Whitehead, R.E. Alkali/alumina molar ratio trends in altered granitoid rocks hosting porphyry and related deposits. *Explor. Min. Geol.* **2010**, *19*, 13–22. [[CrossRef](#)]
43. Leitch, C.H.B.; Lentz, D.R. The gresens approach to mass balance constraints of alteration systems. In *Alteration and Alteration Processes Associated with Ore-Forming Systems*; Geological Association of Canada: St. John's, NL, Canada, 1994; Volume 11, pp. 161–192.
44. Lentz, D.R.; Gregoire, C. Petrology and mass-balance constraints on major-, trace-, and rare-earth-element mobility in porphyry-greisen alteration associated with the epizonal True Hill granite, southwestern New Brunswick, Canada. *J. Geochem. Explor.* **1995**, *52*, 303–331. [[CrossRef](#)]
45. Madeisky, H.E. Quantitative Analysis of Hydrothermal Alteration: Applications in Lithochemical Exploration. Doctoral Dissertation, University of London, London, UK, 1996.
46. Aiuppa, A.; Allard, P.; D'Alessandro, W.; Michel, A.; Parello, F.; Treuil, M.; Valenza, M. Mobility and fluxes of major, minor and trace metals during basalt weathering and groundwater transport at Mt. Etna Volcano (Sicily). *Geochim. Cosmochim. Acta* **2000**, *64*, 1827–1841. [[CrossRef](#)]
47. Large, R.R.; Gemmel, J.B.; Paulick, H.; Huston, D.L. The alteration box plot: A simple approach to understanding the relationship between alteration mineralogy and lithochemistry associated with volcanic-hosted massive sulfide deposits. *Econ. Geol.* **2001**, *96*, 957–971. [[CrossRef](#)]
48. Kirschbaum, A.; Martinez, E.; Pettinari, G.; Herrero, S. Weathering profiles in granites, Sierra Notre (Cordoba, Argentina). *J. South Am. Earth. Sci.* **2005**, *19*, 479–493. [[CrossRef](#)]
49. Sipahi, F.; Sadıklar, M.B. The alteration mineralogy and mass change of the Zigana (Gümüşhane) volcanics of NE Turkey. *Geol. Bull. Turk.* **2010**, *53*, 97–128.
50. Akaryalı, E.; Tüysüz, N. The genesis of the slab window-related Arzular low-sulfidation epithermal gold mineralization (Eastern Pontides, NE Turkey). *Geosci. Front.* **2013**, *4*, 409–421. [[CrossRef](#)]
51. Giggenbach, W.F. Mass transfer in hydrothermal alteration systems—a conceptual approach. *Geochim. Cosmochim. Acta* **1984**, *48*, 2693–2711. [[CrossRef](#)]
52. Giggenbach, W.F. Geothermal solute equilibria: Derivation of Na-K-Mg-Ca geoindicators. *Geochim. Cosmochim. Acta* **1988**, *52*, 2749–2765. [[CrossRef](#)]

53. Stanley, C.R. Graphical investigation of lithochemical variations using molar element ratio diagrams: Theoretical foundation. In *Lithochemical Exploration for Metasomatic Zones Associated with Hydrothermal Mineral Deposits Using Molar Element Ratio Analysis*; Stanley, C.R., Ed.; Short Course Notes; Mineral Deposits Research Unit, Lithochemical Exploration Research Project, University of British Columbia: Vancouver, BC, Canada, 1998; pp. 63–103.
54. Stanley, C.R. Molar element ratio analysis of lithochemical data: A toolbox for use in mineral exploration and mining. *Geochem. Explor. Environ. Anal.* **2020**, *20*, 233–256. [[CrossRef](#)]
55. Okay, A.İ.; Tüysüz, O. Tethyan sutures of northern Turkey. In *Mediterranean Basins: Tertiary Extension within the Alpine Orogen*; Durand, B., Jolivet, L., Horvath, F., Seranne, M., Eds.; Special Publication 156; Geological Society: London, UK, 1999; pp. 475–515.
56. MTA. *General and Economic Geology of the Biga Peninsula*; Special Publication Series 28; MTA: Ankara, Turkey, 2012; p. 326. (In Turkish)
57. Şengör, A.M.C.; Yılmaz, Y. Tethyan evolution of Turkey: A plate tectonic approach. *Tectonophysics* **1981**, *75*, 181–241. [[CrossRef](#)]
58. Richards, J.P. Tectonic, magmatic, and metallogenic evolution of the Tethyan Orogen: From subduction to collision. *Ore Geol. Rev.* **2015**, *70*, 323–345. [[CrossRef](#)]
59. Aldanmaz, E.; Pearce, J.A.; Thirlwall, M.F.; Mitchell, J.G. Petrogenetic evolution of late Cenozoic, post collision volcanism in western Anatolia, Turkey. *J. Volcanol. Geotherm. Res.* **2000**, *102*, 67–95. [[CrossRef](#)]
60. Altunkaynak, Ş.; Genç, Ş.C. Petrogenesis and time-progressive evolution of the Cenozoic continental volcanism in the Biga Peninsula, NW Anatolia. *Lithos* **2008**, *102*, 316–340. [[CrossRef](#)]
61. Ketin, İ. Anadolu'nun tektonik birlikleri. *Bull. Miner. Res. Explor.* **1966**, *66*, 20–34.
62. Yılmaz, Y. Comparison of young volcanic associations of western and eastern Anatolia under compressional regime: A review. *J. Volcanol. Geotherm. Res.* **1990**, *44*, 69–87. [[CrossRef](#)]
63. Şengör, A.M.C.; Lom, N.; Sunal, G.; Zabcı, C.; Sancar, T. The Phanerozoic palaeotectonics of Turkey. Part I: An inventory. *Mediterr. Geosci. Rev.* **2019**, *1*, 91–161. [[CrossRef](#)]
64. Okay, A.İ.; Siyako, M.; Bürkan, K.A. Geology and tectonic evolution of the Biga Peninsula. *Turk. Assoc. Pet. Geol. Bull.* **1990**, *2*, 83–121, (In Turkish with English Abstract).
65. Göncüoğlu, M.C. Introduction to the geology of Turkey: Geodynamic evolution of the pre-Alpine and Alpine terranes. In *General Directorate of Mineral Research and Exploration Monographs Series*; MTA: Ankara, Turkey, 2010; p. 66. ISBN 978-605-4075-74.
66. Topuz, G.; Altherr, R.; Schwartz, W.H.; Dokuz, A.; Meyer, H.P. Variscan amphibolites-facies rocks from the Kurtoğlu metamorphic complex (Gümüştane area, Eastern Pontides, Turkey). *Int. J. Earth Sci.* **2007**, *96*, 861–873. [[CrossRef](#)]
67. Okay, A.İ.; Satir, M.; Siebel, W. Pre-Alpidic Palaeozoic and Mesozoic orogenic events in the eastern Mediterranean region. In *European Lithosphere Dynamics. Geological Society; Memoirs*: London, UK, 2006; Volume 32, pp. 389–405.
68. Delaloye, M.; Bingöl, E. Granitoids from western and northwestern Anatolia: Geochemistry and modeling of geodynamic evolution. *Int. Geol. Rev.* **2000**, *42*, 241–268. [[CrossRef](#)]
69. Okay, A.İ.; Satir, M. Coeval plutonism and metamorphism in a Latest Oligocene metamorphic core complex in northwest Turkey. *Geol. Mag.* **2000**, *137*, 495–516. [[CrossRef](#)]
70. Okay, A.İ.; Monod, O.; Monie, P. Triassic blueschists and eclogites from northwest Turkey: Vestiges of the Paleo-Tethyan subduction. *Lithos* **2002**, *64*, 155–178. [[CrossRef](#)]
71. Okay, A.İ.; Göncüoğlu, C. The Karakaya complex: A review of data and concepts. *Turk. J. Earth Sci.* **2004**, *13*, 77–95.
72. Chesser Resources. *Annual Report*; Chesser Resources Limited: Çanakkale, Turkey, 2012.
73. Tümad Mining. *Annual Report, 10*; Tümad Mining Industry and Trade Inc.: Çanakkale, Turkey, 2020.
74. Okay, A.İ.; Satir, M. Upper Cretaceous eclogite-facies metamorphic rocks from the Biga Peninsula, northwest Turkey. *Turk. J. Earth Sci.* **2000**, *9*, 47–56.
75. Dönmez, M.; Akçay, A.E.; Genç, Ş.C.; Acar, Ş. Middle-upper Eocene volcanism and marine ignimbrites in the Biga Peninsula. *Bull. Miner. Res. Explor.* **2005**, *131*, 49–61.
76. Erenoğlu, O. Chrono-Stratigraphic Position of Eocene, Oligo-Miocene Volcanics around Dededag (Beyçayır-Çanakkale) and Their Importance for Regional Volcanism in the Biga Peninsula. Ph.D. Thesis, Çanakkale Onsekiz Mart University, Çanakkale, Turkey, 2014; p. 217.
77. Hedenquist, J.W. Observations on the Kestanelik and Karaayi Prospects, Biga Peninsula, Turkey. In *Annual Report*; Chesser Resources Limited: Çanakkale, Turkey, 2012.
78. Gülyüz, N.; Shipton, Z.K.; Kuşcu, İ.; Lord, R.A.; Kaymakçı, N.; Gülyüz, E.; Gladwell, D.R. Repeated reactivation of clogged permeable pathways in epithermal gold deposits: Kestanelik epithermal vein system, NW Turkey. *J. Geol. Soc.* **2018**, *175*, 509–524. [[CrossRef](#)]
79. Gülyüz, N.; Shipton, Z.K.; Kuşcu, İ. Multiphase deformation, fluid flow and mineralization in epithermal systems: Inferences from structures, vein textures and breccias of the Kestanelik epithermal Au-Ag deposit, NW Turkey. *Turk. J. Earth Sci.* **2023**, *32*, 75–95. [[CrossRef](#)]
80. Brown, G.; Brindley, G.W. X-ray diffraction procedures for clay mineral identification. In *Crystal Structure of Clay Minerals and Their X-ray Identification*; Brindley, G.W., Brown, G., Eds.; Mineralogical Society: London, UK, 1980.
81. Celenk, O.; Flores, R.A.; dela Cruz, A.P., Jr. Geochemical characterization of epithermal alteration in Southeast Negros, Philippines. *J. Geochem. Explor.* **1987**, *27*, 189–211. [[CrossRef](#)]

82. Berger, B.R. Geologic-geochemical features of hot-spring precious-metal deposits. In *Geologic Characteristics of Sediment- and Volcanic-Hosted Disseminated Gold Deposits-Search for an Occurrence Model*; Tooker, E.W., Ed.; U.S. Geological Survey Bulletin 1646; U.S. Government Printing Office: Washington, DC, USA, 1985; pp. 47–53.
83. Hedenquist, J.W.; Reid, F. *Epithermal Gold*. *Earth Resources Foundation*; University of Sydney: Sydney, Australia, 1985; 31p.
84. Turner, S. Fluid inclusion, alteration and ore mineral studies of an epithermal vein system: Mount Kasi, Vanua Levu, Fiji. In *Proceedings of the Symposium 5: Volcanism, Hydrothermal Systems and Related Mineralization, International Volcanological Congress, Hamilton, New Zealand, 1–9 February 1986; Volume 5*, pp. 87–94.
85. Sverjensky, D.A. Europium redox equilibria in aqueous solution. *Earth Planet. Sci. Lett.* **1984**, *67*, 70–78. [[CrossRef](#)]
86. Yongliang, X.; Yusheng, Z. The mobility of rare-earth elements during hydrothermal activity: A review. *Chin. J. Geochem.* **1991**, *10*, 295–306. [[CrossRef](#)]
87. Poitrasson, F.; Pin, C.; Duthou, J.L. Hydrothermal remobilization of rare earth elements and its effect on Nd isotopes in rhyolite and granite. *Earth Planet. Sci. Lett.* **1995**, *130*, 1–11. [[CrossRef](#)]
88. Boynton, W.V. Cosmochemistry of the rare earth elements: Meteorite studies. Chapter 3. *Dev. Geochem.* **1984**, *2*, 63–114.
89. Barrett, T.; Cattalani, S.; MacLean, W.H. Volcanic litho-geochemistry and alteration at the Dalbride massive sulphide deposits, Noranda Quebec. *J. Geochem. Explor.* **1993**, *48*, 135–173. [[CrossRef](#)]
90. Van Gerven, M. Geochemische Nebengesteins Alterationen und Erfassung Signifikanter Zonierungen im Bereich des Jade-Erzfeldes, Okinawa, Trog, Japan. Ph.D. Thesis, Freir Universitate, Rohstoff and Umweltgeologie, Berlin, Germany, 1995; p. 186.
91. Buchanan, L.J. Precious metal deposits associated with volcanic environments in the southwest. *Arizona Geol. Soc. Digest* **1981**, *14*, 237–261.
92. Dilekler, G. Mineralization, Textural and Alteration Characteristics of the Şahinli (Sirakayalar and Karatepe) Low Sulfidation Epithermal Deposit (Lapseki, NW Turkey). Master’s Thesis, Middle East Technical University, Ankara, Turkey, 2022; p. 148.
93. Alderton, D.H.M.; Pearce, J.A.; Potts, P.J. Rare earth element mobility during granite alteration: Evidence from southwest England. *Earth Planet. Sci. Lett.* **1980**, *49*, 149–165. [[CrossRef](#)]
94. Palacios, C.M.; Hein, U.F.; Dulski, P. Behaviour of rare earth elements during hydrothermal alteration at the Buena Esperanza copper–silver deposit, northern Chile. *Earth Planet. Sci. Lett.* **1986**, *80*, 208–216. [[CrossRef](#)]
95. Nesbitt, H.W. Mobility and fractionation of rare earth elements during weathering of a granodiorite. *Nature* **1979**, *279*, 206–210. [[CrossRef](#)]
96. Warren, I.; Simmons, S.F.; Mauk, J.L. Whole-rock geochemical techniques for evaluating hydrothermal alteration, mass changes, and compositional gradients associated with epithermal Au-Ag mineralization. *Econ. Geol.* **2007**, *102*, 923–948. [[CrossRef](#)]
97. Michard, A.; Albarede, F. The REE content of some hydrothermal fluids. *Chem. Geol.* **1986**, *55*, 51–60. [[CrossRef](#)]

**Disclaimer/Publisher’s Note:** The statements, opinions and data contained in all publications are solely those of the individual author(s) and contributor(s) and not of MDPI and/or the editor(s). MDPI and/or the editor(s) disclaim responsibility for any injury to people or property resulting from any ideas, methods, instructions or products referred to in the content.